UC Riverside
UC Riverside Electronic Theses and Dissertations

Title

Langmuir Probe Diagnostics in Dusty, Non-Thermal Plasmas

Permalink

https://escholarship.org/uc/item/4484p94s

Author

Woodard, Austin T

Publication Date

2020

Peer reviewed|Thesis/dissertation

UNIVERSITY OF CALIFORNIA
RIVERSIDE

Langmuir Probe Diagnostics in Dusty, Non-Thermal Plasmas

A Dissertation submitted in partial satisfaction
of the requirements for the degree of

Doctor of Philosophy

in

Materials Science & Engineering

by

Austin T. Woodard

June 2020

Dissertation Committee:
        Dr. Lorenzo Mangolini, Chairperson
        Dr. Richard Wilson
        Dr. Sinisa Coh

The Dissertation of Austin T. Woodard is approved:

Committee Chairperson

University of California, Riverside

I acknowledge all of my labmates. They were always there whenever I needed their help, and they always provided it selflessly and efficiently.

I acknowledge my committee members for providing their constructive feedback throughout my graduate studies at UCR.

Finally, I would like to acknowledge my advisor, Dr. Lorenzo Mangolini, for his implacable spirit, that which never faltered during frustration nor the unknown, and his inspiring drive, a continuous reminder of the mentality necessary for success in the academic world and otherwise; I could not have asked for a better advisor to guide me through my PhD.

For my family.

ABSTRACT OF THE DISSERTATION

Langmuir Probe Diagnostics in Dusty, Non-thermal Plasmas

by

Austin T. Woodard

Doctor of Philosophy, Graduate Program in Materials Science & Engineering
University of California, Riverside, June 2020
Dr. Lorenzo Mangolini, Chairperson

Non-thermal plasmas, at their most ideal, are well understood; the realistic non-thermal

plasma, that which is utilized across nearly all semi-conductor related industries as well

as extensively in academia, remains thoroughly lacking that understanding, specifically,

the non-thermal plasmas which synthesize and/or contain particulate matter, so-called

dusty plasmas. This work addresses the marked difficulty in probing such discharges,

presenting a design which results in a much more forgiving and simple system to probe

and investigate—one which contains solely conductive dust and inert gases. This work

studies potential conductive dust candidates and subsequent synthesis methods that

adhere to these restrictions, resulting in a separate non-thermal plasma technique for the

synthesis and injection of graphitic nanoparticles, as well as the inert gas, into the probed

discharge. This work presents a home-built Langmuir probe capable of comprehensive

measurements of the electron energy distribution function and important plasma

parameters, with no measured degradation caused by a build-up of graphitic nanoparticles

on the probe surface. This work confirms that the presence of dust leads to a decrease in

electron density and, thus, an increase in the average electron temperature. Finally, this

work studies the phenomenon of nanoparticle trapping, presents the first direct measurement of the particle floating potential in a dusty plasma, and represents a step towards understanding the incredibly complex effect of plasma-dust interactions.

Table of Contents

List of Figures

Chapter 1: Introduction & Background

Chapter 2: On the non-thermal plasma synthesis of Nickel Nanoparticles

Chapter 3: Graphitization of carbon particles in a non-thermal plasma reactor

List of Equations

Chapter 4: Langmuir probe characterization of an Ar-H$_2$ non-thermal plasma loaded with carbon nanoparticles

Chapter 5: Electron emission from particles strongly affects the electron energy distribution in dusty plasmas

Chapter 1: Introduction & Background

1.1 Introduction

Much of the knowledge on gas discharges has come from experimental approaches using Langmuir probes and spectroscopic techniques in ideal, inert gas only environments[1-3]. However, non-thermal plasmas are employed ubiquitously across both academia and industry—from research endeavors into nanoparticle synthesis[4-6], to employing non-thermal plasmas in Plasma Enhanced Chemical Vapor Deposition (PECVD) systems for semiconductor manufacturing—where the realistic plasma environment does not clearly match the ideal. This dissertation focuses on designing and employing a system to enable a simple and forgiving environment in which to investigate the interaction between non-thermal, low-pressure plasma and nanoparticles by applying the foundational techniques of Langmuir probes to further bridge the gap between ideal and realistic understanding of said interaction.

1.2 Theory of Langmuir Probes

Some of the earliest examples of probes inside discharges were attempts to measure the potential inside a cathode arc[7]. Langmuir et. al.[8] later expanded upon the theory of using such probes in discharges, demonstrating that spherical and cylindrical probes can provide detailed information on the potential of the plasma, the density of charged species inside the plasma, and the temperature of the electrons. Further refinement of probe diagnostics by Druyvesteyn[9] allowed for the determination of the Electron Energy Distribution Function (EEDF, F(E)) directly from the second derivative of the probe current, through the following relationship:

$$F(E) = \frac{4}{e^2 A_p} \left(\frac{mV}{2e}\right)^{1/2} \frac{d^2 I}{dV^2} \qquad (1)$$

Where e is the charge of an electron, A_p is the area of the probe, m is the mass of an electron, V is the probe voltage with respect to the potential of the plasma, and I is the probe current.

To fully consider how powerful a technique the Druyvestyn method is, one must realize the information obtainable from the EEDF. For this, we must first consider that an electron gas in plasma is described by the electron-distribution function (EDF)[10,11]:

$$EDF = f(t, \vec{r}, \vec{v}) \qquad (2)$$

From this, we have the relationship for obtaining the electron density, N from the following:

$$N(t, \vec{r}) = \int f(t, \vec{r}, \vec{v}) d\vec{v} \qquad (3)$$

However, we must reach an expression of the EDF in terms of energy, e.g., an expression of the EEDF. If the discharge is assumed to be isotropic, this relationship holds:

$$f(t, \vec{r}, \vec{v}) = f_0(t, \vec{r}, v) \qquad (4)$$

Where $\vec{r}$ is the space-coordinate vector and $\vec{v}$ is the velocity vector. If also making the assumption that:

$$v = \sqrt{\frac{2\varepsilon}{m}} \qquad (5)$$

where ε is electron kinetic energy and m is the mass of an electron, one arrives at the following expression for the EEDF:

$$F(t, \vec{r}, \varepsilon) = 4m^{-\frac{3}{2}} \sqrt{2\pi} \sqrt{\epsilon} f_0 \left(t, \vec{r}, \sqrt{\frac{2\varepsilon}{m}} \right) \qquad (6)$$

In addition, because the angular distribution for electrons is the same in any direction, f_0 and F both contain the same information regarding the electron gas inside the plasma, the following relationship for electron density holds true:

$$N = \int_0^\infty F(\varepsilon)d\varepsilon \qquad (7)$$

With the effective electron temperature, T_e being a measure of the average electron energy the following relationship for electron temperature is as follows:

$$T_e = \frac{2}{3}N^{-1}\int_0^\infty \varepsilon F(\varepsilon)d\varepsilon \qquad (8)$$

If one can obtain the EEDF, one also immediately obtains the electron density and electron temperature. Furthermore, one can transform directly the EEDF into the electron energy probability function, the more common representation found in literature, from the following:

$$F(\varepsilon) = \sqrt{\varepsilon}f(\varepsilon) \qquad (9)$$

The last remaining plasma characteristic of importance is the ion density. Thankfully, Langmuir et. al. derived an expression for ion density that allows its determination directly from the probe I-V[8], and Chen et. al. further developed the theory of probe ion-collection in 1965[12,13]. To do this, one must fit the ion current to the following expression:

$$I_{ion} = n_{ion}2eA_p\sqrt{\frac{2e|V_p - V|}{m_{ion}}} \qquad (10)$$

Where I_{ion} is the ion current, n_{ion} is the ion density, V_p is the plasma potential, V is the collected probe potential, and m_{ion} is the ion mass. Figure 1.1 depicts an I-V collected in an pristine plasma environment; the blue-shaded region (the ion saturation regime) indicates the portion of the voltage sweep where solely ion current is collected; the orange-shaded region (the electron-retardation regime) indicates the portion of the voltage sweep where, although still negative with respect to the plasma potential, the collected current has both ion and electron components; the red-shaded region (the electron saturation regime) indicates the portion of the voltage sweep where the probe potential is positive with respect to the plasma potential, and so the current collected is solely electron current—the boundary between the orange and red shaded regions, where there is a "knee," or change or curvature in the I-V, is indicative of the plasma potential. Fitting the ion saturation regime of the I-V to Eq. (9) allows one to calculate the ion density, given a known m_{ion}. Therefore, the Druyvestyn methods allows one to obtain all the relevant plasma

characteristics directly from the probe *I-V* characteristic and highlights why cylindrical Langmuir probes are still the main diagnostic tool used by both academia and industry.
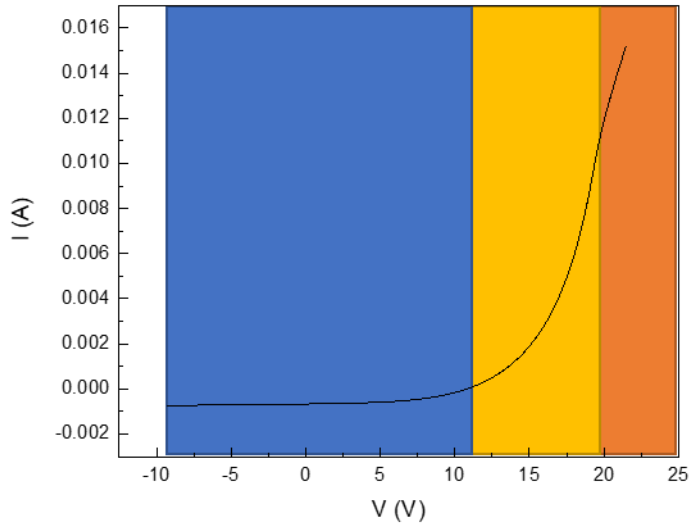
Figure 1.1. A typical *I-V* characteristic obtained from a Langmuir probe, with the ion saturation regime in blue, electron retardation regime in orange, and electron saturation regime in red.

1.3 Probe design requirements

While Langmuir probes have extensively aided in furthering the understanding of fundamental plasma physics, this technique is not without its drawbacks and limitations—most notably, that Langmuir probes are intrusive and require careful design to neither be destroyed nor perturb the plasma. The design of Langmuir probes, as can be expected, is a subject of research well-explored and documented[14-16]. The most basic of probes need only satisfy the underlying assumptions of the classical Langmuir probe diagnostics which require a probe small enough in order to ignore unaccounted for perturbations of the plasma[17,18]. This is more easily understood through the following relationship:

$$d_p, d_{ph}, \lambda_D \ll \lambda_e \tag{11}$$

Where d_p is the probe diameter, d_{ph} is the probe holder diameter, λ_D is the electron debye length in the plasma, and λ_e is the electron relaxation length. The electron debye length in a plasma (generally around 0.1mm, depending on plasma parameters) can be expressed as the following:

$$\lambda_D = \sqrt{\frac{\epsilon_0 k_B T_e}{n_e e^2}} \tag{12}$$

Where ϵ_0 is the permittivity of free space, k_B is the Boltzmann constant, and n_e is the electron density. The electron relaxation length for weakly ionized plasmas (generally in the range of 20 cm to 2 cm depending on plasma parameters and electron energy) can be expressed as follows[3]:

$$\lambda_e \approx 100 \frac{1}{n_e s_e(v)} \tag{13}$$

Where $s_e(v)$ is the momentum transfer scattering cross-section for electrons. Essentially, this is to satisfy the constraint that the plasma is collision-less with respect to the probe, e.g. the probe is designed such that it is sufficiently small enough, when compared to the average length an electron will travel before a collision event, that electrons are not lost to the probe. Figure 1.2 depicts a typical probe design that satisfies this requirement, colloquially known as telescopic probe.
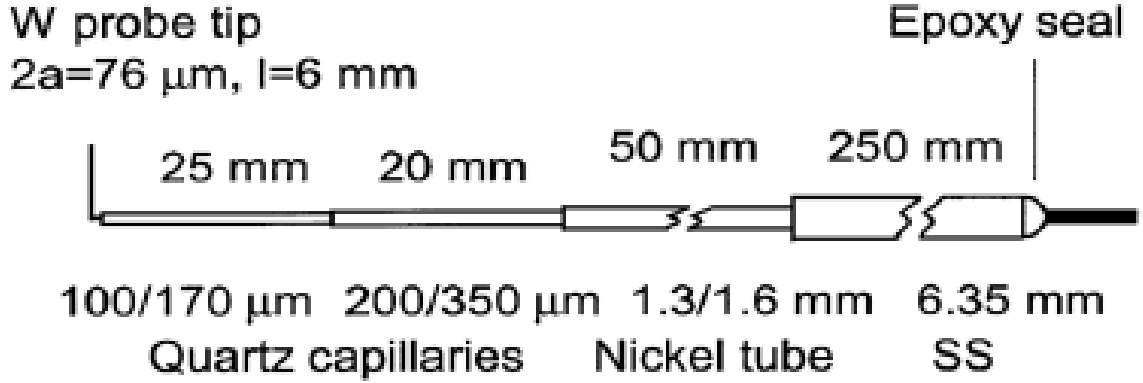
Figure 1.2. Telescopic probe used for EEDF measurements, reproduced from ref. [19].

The final requirement for probe design revolves not around the underlying theory, but instead a well-documented issue of plasma oscillations causing significant distortions of the *I-V* probe characteristic[20-22], and thus the second-derivative of this characteristic which is necessary for determining the EEDF, as shown earlier. To combat these plasma oscillations, the following inequality needs to be satisfied[19]:

$$\left|\frac{Z_{pr}}{Z_f}\right| \le \frac{(0.3 - (0.5)T_e}{|eV_{prf}|} \qquad (14)$$

Where Z_{pr} is the impedance between the probe and plasma, Z_f is the attached electric filter impedance, and V_{prf} is the rms rf plasma potential. To satisfy this inequality, Z_{pr} needs to be minimized and Z_f maximized.

Firstly, the most straightforward way in which to minimize Z_{pr} without complicating the biasing procedure or increasing the complexity of the probe circuitry, is to introduce a passive filtering method. This involves what is defined as a "shunting electrode" placed at rf equipotential to the probe (or more simply, placed in close proximity to the probe)[23,24], in connection to a capacitor that is much larger than the probe-plasma

capacitance while remaining small enough to not produce a noticeable displacement current to the collected probe current; in practice, reliably measuring the probe-plasma capacitance is difficult, and assumed to be around a 1pF, therefore, a capacitor from a few hundred pF to tens of nF is experimentally found to be acceptable if the area of the shunting electrode is much larger than the area of the probe[25], as this would decrease Z_{pr} by as much as one to two orders of magnitude. As an example, a probe with a radius of .127μm and height of 10mm equipped with a shunting electrode having a radius of 1cm and height of 2cm would be more than sufficient to allow a capacitor spanning the aforementioned capacitance range while satisfying the requirement to minimize Z_{pr}.

Secondly, maximizing Z_f requires the addition of notch filters, or "chokes", tuned to the harmonics relevant to the system at hand. Self-resonant inductive chokes (inductors designed such that the inherent inductance and capacitance form a notch filter for specific frequencies) are the easiest to use in such an endeavor, as such devices have relatively large bandwidths, with capacitances tuned to be near 1pF, resulting in a large filter impedance, as can be seen with the following equation:

$$Z_f = Q(\omega C)^{-1} \qquad (15)$$

Determining which frequencies to block using these self-resonant inductive chokes depends entirely on the frequency of the power generating the discharge. As an example, a 13.56 MHz driven discharge (a quite common radio frequency chosen in laboratory and industrial endeavors) might require a series of inductive chokes accounting for the first harmonic at the least, and potentially the second and third harmonics depending on the precision needed and clarity of the second derivative of the *I-V* probe characteristic. Figure 1.3 shows how necessary satisfying inequality (14) is, as the second derivative is extremely distorted without the addition of the aforementioned suggested solutions.
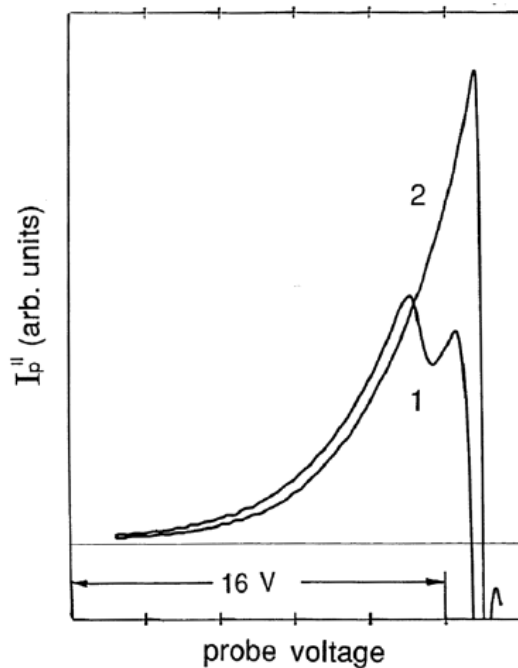
Figure 1.3. Second derivative of the probe characteristic in a Helium discharge, (1) without the filter elements discussed, and (2) with complete filtering and satisfaction of inequality (15). Reproduced from ref. [19].

1.4 Dust-rich discharge complications

Employing a simple Langmuir probe with all the design requirements as stipulated in 1.3 is sufficient for investigating "pristine" discharges, that is, those plasmas that contain solely inert gases. However, expanding this technique to so-called "dusty plasmas", those which contain not only inert gases but also particulate matter or "dust", is attractive because, as stated, these dusty plasmas are used ubiquitously in academia and industry, with not much understanding of how the plasma-dust interactions effect the plasma behavior and parameters. Experimentally, employing Langmuir probes in such dust-containing environments is challenging, most notably due to issue of dust accumulation on the probe surface which not only increases the area of the probe, but also leads inevitably to a marked increase of the resistance of the probe due to the coating of insulating particles. Most literature attempting to probe dusty plasmas using Langmuir probes has been in silicon-forming discharges[26-29], with clever probe design or implementation to ignore the issue of *I-V* distortion caused by the accumulation of dust on the surface of the probe, such as only exposing the probe to the dust-containing plasma for very small time windows, paired with fast-voltage sweeps or probe heating, but these introduce problems of low signal-to-noise ratios and lost resolution of the obtained EEDF or induced thermionic effects, respectively.

Additionally, much of these experimental endeavors occur in environments containing the precursor gas used to synthesize the dust[26,30-33] further complicating interpretation of the obtained EEDF and enhancing the problem of potential *I-V* distortion through not just dust accumulation but film formation on the probe surface.

1.5 Designing a more forgiving dusty plasma environment

This dissertation aims to create a more forgiving plasma environment, compared to those more complicated systems indicated earlier, in which to employ a simple Langmuir probe to investigate the effect of plasma-dust interactions. To this end, there are two main conditions that must be satisfied:

(1) Obtaining a modular method of synthesizing conductive dust that allows for direct injection of the synthesized dust into the probed plasma environment.

(2) Ensuring that the modular method outputs only the conductive dust and inert gas, with no remaining precursor.

To clarify, (1) would allow for dust to accumulate on the probe tip without significant distortion of the obtained *I-V* so long as the dust is truly conductive and does not form too thick a coating; (2) would allow for the interpretation of the obtained data to ignore the effects of nucleation kinetics and/or the effects of the precursor gas being inside the plasma environment. Thus, these two conditions create a forgiving environment in which the only constituent that may affect the plasma behavior and parameters is that of plasma-dust interactions, with no need of clever accommodations to combat a distortion-inducing coating forming on the probe tip.

Chapter 2 is the first attempt at satisfying (1), through a modular non-thermal plasma reactor for the synthesis of dust, namely Ni nanoparticles. However, Chapter 2 dictates the results that while metallic Ni nanoparticles are obtained, the nanoparticles are not of simplistic design (instead, a core-shell structure is formed), not solely of Ni (as there

are additional, unwanted carbonaceous particles synthesized), nor does this attempt satisfy (2) as the precursor is not fully consumed in the synthesis of dust. In Chapter 3, this synthesis technique is refined and amended for the production of purely carbonaceous nanoparticles via the precursor acetylene; highly graphitic nanoparticles are obtained with 100% of the precursor consumed, resulting in an output of solely inert gas and conductive dust, satisfying both (1) and (2). Chapter 4 depicts the design and implementation of the home-made Langmuir probe, the lack of distortion of the obtained data from the inevitable coating of conductive nanoparticles, as well as the effects of plasma-dust interaction on the relevant plasma parameters. Chapter 5 further studies this interaction at much lower pressure (to observe more marked effects on the plasma parameters), describes the phenomenon of nanoparticle trapping, and is the first direct measurement of nanoparticle floating potential through the emergence of a peak in the obtained EEDFs attributed to the nanoparticles acting as distributed electron emitters.

1.5 References

(1)   Smith, J. D. & Schwar, M. J. R. *Electrical Probes for Plasma Diagnostics* (1970).

(2)   Mott-Smith, H. M. & Langmuir, I. *Gen. Electr. Rev.* 449, 538, 616, 762, 810 (1924).

(3)   Demidov, V. I., Ratynskaia, S. & Rypdal, K. *Rev. Sci. Instrum.* **73,** 3409 (2002).

(4)   Yasar-Inceoglu, O., Lopez, T., Farshihagro, E. & Mangolini, L. *Nanotechnology* **23**, 255604 (2012).

(5)   Kortshagen, U. R. *et al. Chem. Rev.* **116**, 11061–11127 (2016).

(6)   Alvarez Barragan, A., Ilawe, N. V., Zhong, L., Wong, B. M. & Mangolini, L. *J. Phys. Chem. C* **121**, 2316–2322 (2017).

(7)   Stark, J., Retschinky, T. & Schaposchnikoff A. *Ann. Phys.* **323** (1905).

(8)   Mott-Smith, H. M. & Langmuir, I. *Phys. Rev.* **28** (1926).

(9)   Druyvesteyn, M. J. Der Niedervoltbogen. *Z. Phys* **64**, 781–798 (1930).

(10)   Shkarofsky, I.P., Johnston, T.W. & Bachynski, M.P., *The particle kinetics of plasmas.* (1966)

(11)   Lieberman, M.A. & Lichtenberg, A.J., *Principles of plasma discharges and materials processing.* (2005)

(12)   Chen, F. F. *J. Appl. Phys.* **36** (1965).

(13)   Chen, F. F. *J. Nucl. Energy, Part C Plasma Phys.* **7** (1965).

(14)   Sudit, I. D. & Chen, F. F. *Plasma Sources Sci. Technol.* **3** (1994).

(15)   Piejak, R. B. *Plasma Sources Sci. Technol.* **1** (1992).

(16)   Cherrington, B. E. *Plasma Chemistry and Plasma Processing.* **2**, 113–140 (1982).

(17)   Waymouth, J. F. .*Journal of Applied Physics.* **4492** (2007).

(18)   Little, R. G. & Waymouth, J. F. *The Physics of Fluids.* **9**, 801-808 (2017).

(19)   Godyak, V. A. & Demidov, V. I. *J. Phys. D. Appl. Phys.* **44** (2011).

(20)   Paranjpe, A. P., McVittie, J. P. & Self, S. A. *J. Appl. Phys.* **67** (1990).

(21)   Flender, U., Nguyen Thi, B. H., Wiesemann, K., Khromov, N. A. & Kolokolov, N. B. *Plasma Sources Sci. Technol.* **5**, (1996).

(22)   Godyak, V. A. *Plasma Sources Sci. Technol.* **20** (2011).

(23)   Godyak, V.A., *Plasma-Surface Interaction and Processing of Materials*. p.95. (1990)

(24)   Demidov, V.I., Kolokolov, N.B. & Kudryavtsev, A.A. *Probe Methods for Low-Temperature Plasma Investigations*. (1996)

(25)   Chatterton, P. A., Rees, J. A., Wu, W. L. & AL-Assadi, K. *Vacuum* (1991).

(26)   Bilik, N., Anthony, R., Merritt, B. A., Aydil, E. S. & Kortshagen, U. R. *J. Phys. D. Appl. Phys.* **48** (2015).

(27)   Bose, S., Kaur, M., Chattopadhyay, P. K. & Ghosh, J. *J. Plasma Phys.* **83,** 1–27 (2017).

(28)   Klindworth, M., Arp, O. & Piel, A. *Rev. Sci. Instrum.* **78** (2007).

(29)   Thomas, E. & Watson, M. *Phys. Plasmas* **6** (1999).

(30)   Okada, K., Komatsu, S. & Matsumoto, S. *J. Vac. Sci. Technol. A Vacuum, Surfaces, Film.* **17** (1999).

(31)   Weiler, M., Kleber, R., Jung, K. & Ehrhardt, H. *Diam. Relat. Mater.* **1** 121–126 (1992).

(32)   Awakowicz, P., Schwefel, R., Werder, M. & Kasper, W. *Surf. Coat. Technol.* **98**, 1020–1026 (1998).

Chapter 2: On the non-thermal plasma synthesis of Nickel nanoparticles

2.1 Introduction

As stated in Chapter 1, one of the main tenets of this dissertation is to address the inherent difficulties in employing Langmuir probes in dusty plasmas—that is, to reliably and controllably synthesize conductive nanoparticles such that the output of such a system is solely monodisperse, conductive, and pure material with inert gases. Metallic nanoparticles (mNPs), a conductive material family with many synthesis techniques, have also been shown to possess attractive tunable properties paving the way for their utilization in a broad range of applications. A plethora of examples exist: novel non-precious catalysts,[1] magnetic nanomaterials,[2] biomedicine,[3] and optoelectronics devices.[4] Many studies in these fields highlight the crucial role of controlling mNP size, which determines their fundamental physical properties,[5] and is of likewise crucial importance to this dissertation. Hence, the development of novel synthesis routes enabling a fine and straightforward tuning of their structural properties is of major interest in mNPs research as a whole and this specific work. Among several possible candidates, non-thermal plasma-based fabrication techniques have emerged as promising all-gas phase protocols for the synthesis of a broad variety of NPs, including semiconductors,[6] metal oxides,[7] ceramics,[8] and more complex core-shell nanostructures.[9] Such systems can produce particles with tight and controlled size distribution (PSDs) [10] and high-quality crystalline structure [11], while the all-gas phase capabilities prove promising for modularly amending such a system for the use in this dissertation. Metal nanoparticles have been successfully produced using atmospheric pressure plasmas.[12] Among the advantageous properties of

this approach is the fact that the particles appear to be effectively free of surface contamination.[13] As a comparison, liquid phase chemical routes are used routinely to produce, for instance, silver and gold nanoparticles, but this processing route makes use of ligands that inevitably alter the surface properties of the particles and complicate the ability to synthesize pure material. Motivated by these studies, we have investigated the formation of nickel nanoparticles in a continuous flow low pressure non-thermal plasma reactor. Our approach is similar to the one routinely used for silicon nanoparticle synthesis,[11] with the aim of proving that such structure can be produced in a controllable way and with high throughput. An in-depth analysis of the structure, chemical composition and size dispersion of the produced nanopowders is presented. We have found that while nickel particles can be successfully produced, the precursor utilization rate is low and the particles are coated by a carbon shell.

2.2 Experimental Methods

2.2.1: Nickel Nanoparticle Synthesis

Figure 2.1 provides a schematic of the continuous-flow non-thermal plasma reactor. The system comprises a sublimation chamber, modelled roughly after a catalyst bed reactor, a quartz tube vessel (outer and inner diameters equal to 25.4 mm and 20 mm respectively) and a copper-ring cathode connected to a RF source (13.56 MHz). The flange upstream of the powered electrode was grounded and serves as reference electrode in the capacitively coupled plasma discharge. The spacing of the electrodes is 5 cm. The reactor is equipped with an optical emission spectroscopy (OES) setup. The light emission

originating from the plasma volume is collected along a line-of-sight parallel to the long axis of the quartz tube and directed to a monochromator (Oriel Instruments, Cornerstone™ 260 Monochromator) equipped with a silicon photodiode. The spectra are measured with an integration time of 500 ms nm^{-1}. For the samples discussed in this chapter, argon gas was flown at constant flow rate through the sublimation chamber and used as carrier gas. H_2 was injected through a second gas inlet placed downstream of the sublimation chamber. The ignition of the low-pressure RF discharge lead to the formation of energetic species, to the dissociation of Ni(Cp)$_2$, and to the nucleation of Ni nanoparticles. The total pressure in the reactor was held constant at 20 Torr by a pressure-controlled butterfly valve located upstream of the vacuum pump (see Figure 1). Two different gas mixtures were used: 70 sccm Ar and 70 sccm Ar + 30 sccm H_2, indicated in the discussion as *0% H_2* and 3*0% H_2* respectively. The Ni(Cp)$_2$ flow rate was 0.0175 sccm under the assumption that it reaches its equilibrium vapor pressure in the sublimation chamber.[14] The sublimator is at room temperature. RF power values of 20 W and 100 W were used for the Ni NPs synthesis. The particles were collected on a filter composed of a fine stainless steel mesh. For TEM analysis, a TEM grid was anchored to the stainless steel mesh using double-sided carbon tape and the particles were collected directly from the gas stream.
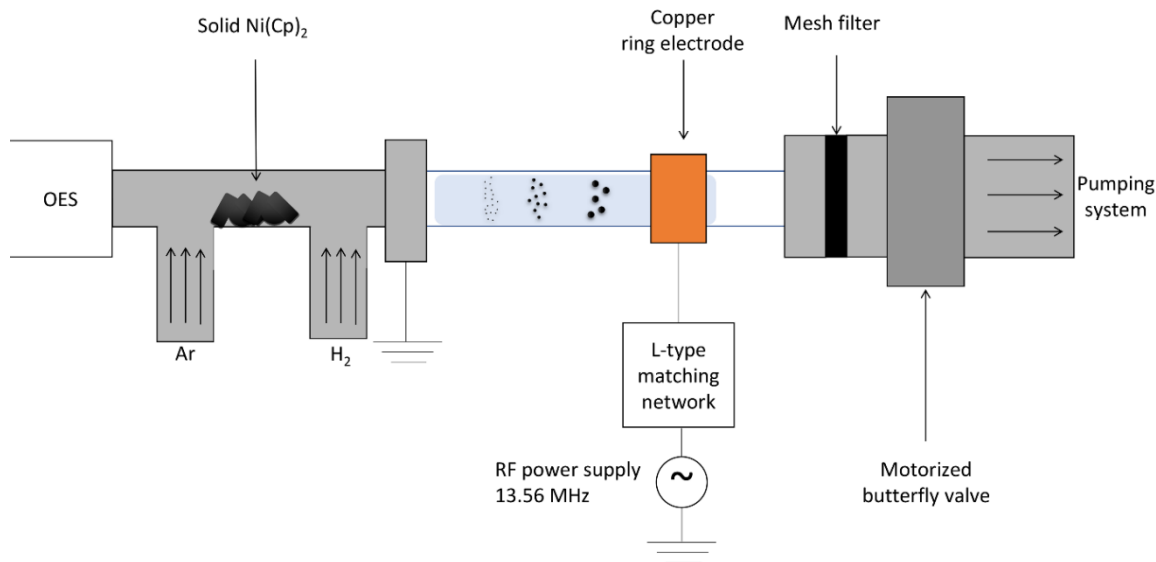
Figure 2.1. Schematic of the setup employed for the synthesis of nickel nanoparticles.

2.2.2 Materials Characterization

TEM imaging and selected-area electron-diffraction (SAED) were carried out with a Tecnai12 microscope. Ni NPs were directly collected on Cu grids placed inside the plasma reactor. A short deposition time of 10 seconds was chosen in order to limit the formation of large particle agglomerates. Particle size frequency count histograms were derived from the analysis of statistical ensembles of 100 nanoparticles with ImageJ software. SEM-EDS analysis was performed with a Nova NanoSEM 450 microscope. The material production yield of the systems was measured with a Sartorius ENTRIS64-1S micro balance.

2.3 Results and Discussion

Ni-based nanomaterials have been synthesized using the combination of parameters delineated in the experimental section. We have first investigated the impact of different levels of the RF power on the NPs fabrication process by employing gas mixtures without H_2. We have found that two different dissociation regimes of $Ni(Cp)_2$ can be induced by changing the value of this process parameter and we have performed a series of SEM-EDS scans to gain insight into the corresponding chemical composition of the as-produced powder. At 100 W, we observe the formation of a carbon-rich nanopowder with a C atomic content of 87.3% (see in Figure 2.2). In this high input power condition, the $Ni(Cp)_2$ cyclopentadienyl (CP) rings are largely dissociated into smaller organic molecules as a result of the relatively low binding energy of the $Ni(Cp)_2$, in the order of 3-4 eV. [15] The opposite scenario holds at low input power —20 W—, with the carbon contribution to the EDS signal undergoing a roughly twofold reduction (see Figure 2.2).
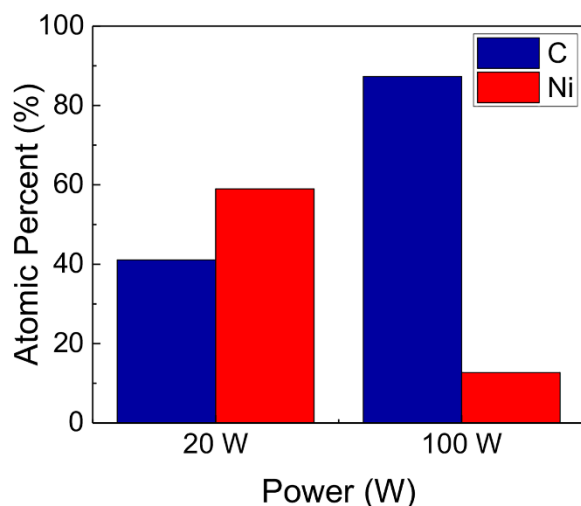
Figure 2.2: EDS analysis of Nickel nanoparticles produced at 20 W and 100 W with 0% H_2

The TEM analysis in Figure 2.3 depicts the structure and PSD of the nanomaterials synthesized at 20 W and 100 W. In the high-resolution micrographs we observe, for both conditions, a heterogeneous mixture of metallic Ni nanoparticles, with well-defined polycrystalline ring features in the corresponding SAED diffraction patterns matching that of metallic Ni, and carbon by-products (see Figure 2.3a and Figure 2.3b). The PSDs are not monodisperse and exhibit a broad and seemingly bimodal distribution, with particle size ranging from few nanometers to 40 nm (see Figure 2.3c and Figure 2.3d). Notably, a large number of Ni particles with an onion-like carbon graphitic shell (see Figure 2.3b) can be identified in the synthesized composites. While obtaining carbon-free mNPs is a challenging endeavor with the current system, these findings suggest a possible application of the current approach as one-step low-temperature strategy for the synthesis of composite catalytic materials. Recent investigations demonstrated the beneficial effect given by the presence of a conductive graphitic carbon shell on Ni nanoparticles enhancing their durability, thermal stability and oxidation resistance.[16]
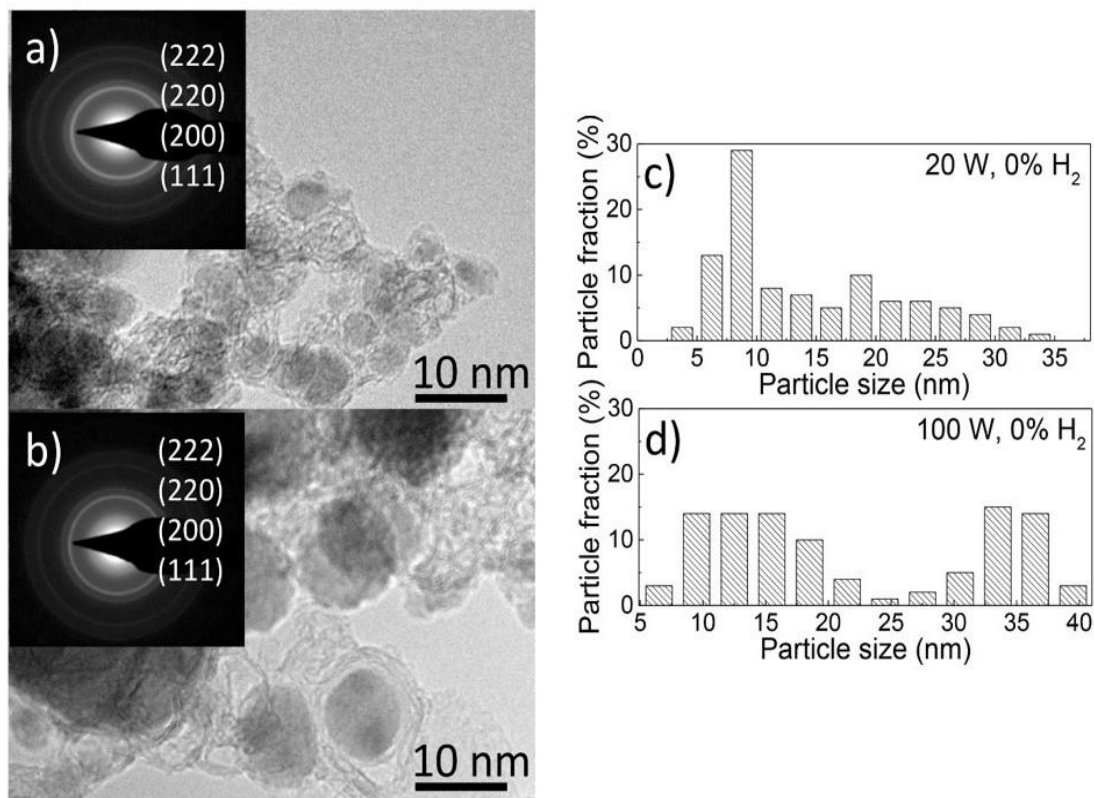
Figure 2.3. Bright field TEM micrographs of Nickel particles synthesized at (a) 20 W and (b) 100 W with 0% H$_2$. The insets illustrate the corresponding SAED patterns, showing polycrystalline diffraction rings (corresponding to the {222}, {220}, {200} and {111} lattice planes of Ni). (c) and (d) shows the PSD of the materials of (a) and (b) respectively.

In an attempt to achieve further control of the chemical composition of the synthesized materials, we investigated the addition of 30% H$_2$ to the gas mixture. The H$_2$-rich atmosphere significantly reduces the C atomic percentage, down to 17% at 20 W and 56.5% at 100 W (see Figure 2.4), as a result of the hydrogen-induced hampering of Ni(Cp)$_2$ dissociation. When the cyclopentadienyl radicals are introduced to a hydrogen-rich

atmosphere, the Cp rings are readily hydrogenated[17] thus preventing further dissociation into base C species.
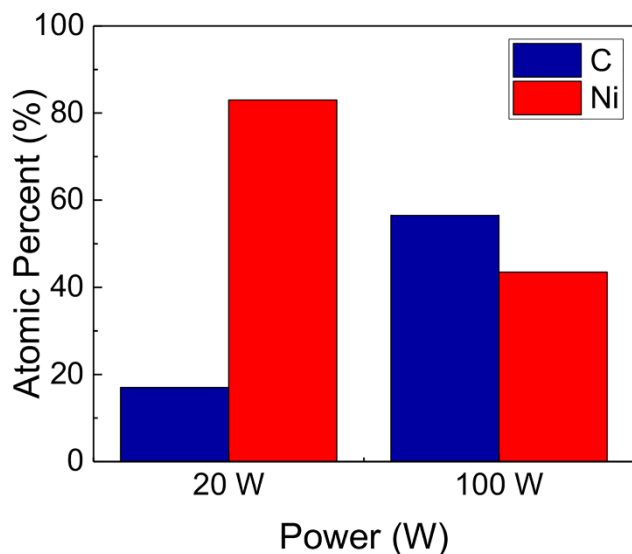
Figure 2.4. EDS analysis of Nickel nanoparticles produced at 20 W and 100 W with 30% H_2.

As shown by the TEM in Figure 2.5, while in these process conditions we can still observe the presence of core-shell Ni-C in the micrographs, the production of carbon nanopowders is significantly reduced, as seen in Figure 2.6. The corresponding PSDs shows an overall tighter and more monodisperse shape, with mean size equal to 3.3 nm at 20 W and 10.9 nm at 100 W and the standard deviation respectively within 20% and 33% of the average dimensions. The data shown so far clearly points to a synergetic role played by the input power and hydrogen dilution in tailoring the properties of the synthesized nanomaterials. The analysis of the spectral emission from the plasma volume provides an approximate idea of the relative variation of the chemical species in the volume of the discharge induced by the variation of these parameters.
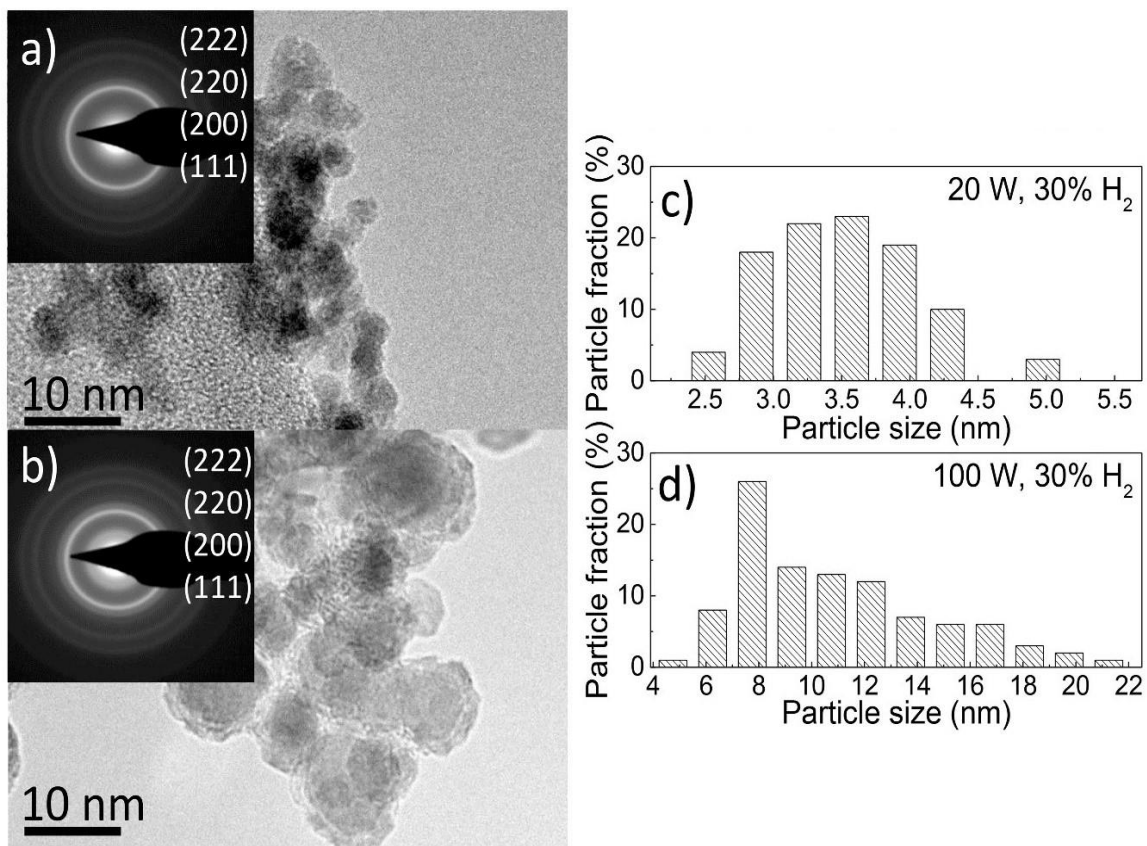
Figure 2.5. Bright field TEM micrographs of Nickel particles synthesized at (a) 20 W and (b) 100 W with 30% H₂. The insets illustrate the corresponding SAED patterns, showing well defined polycrystalline diffraction rings (corresponding to {222}, {220}, {200} and {111} lattice planes of Ni). (c) and (d) shows the PSD of the materials of (a) and (b) respectively.
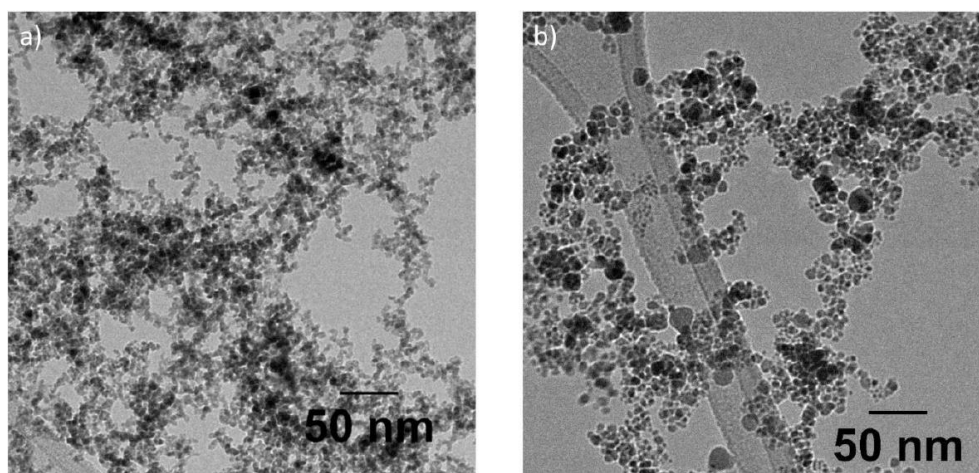
Figure 2.6. Low-magnification bright field TEM micrographs of Nickel particles synthesized at (a) 20 W with 0% H₂ and (b) 100 W with 30% H₂.

Figure 2.7 shows the OES spectra collected at 100 W for 0% H_2 and 30% H_2; the introduction of H_2 in the gas mixture significantly lowers the overall plasma density and, correspondingly, we observe a drop of the emission intensity. The peaks at 469 nm, 513 nm, and 550 nm (see insets in Figure 6a and Figure 6b), attributed to C_2 species,[18] are easily distinguishable for 0% H_2—the experimental condition that produces carbon-rich samples—but become indistinguishable from the noise level at 30% H_2. This supports the previously stated interpretation of the role that hydrogen plays in preventing the further precursor dissociation into smaller organic molecules. Lowering the power to 20 W, we observe the same qualitative trend upon introduction of H_2, (see Figure 2.7c and 2.7d),

but the emission intensity of the plasma discharge is lower with respect to 100 W, due to

a further reduction in plasma density and hence precursor dissociation.
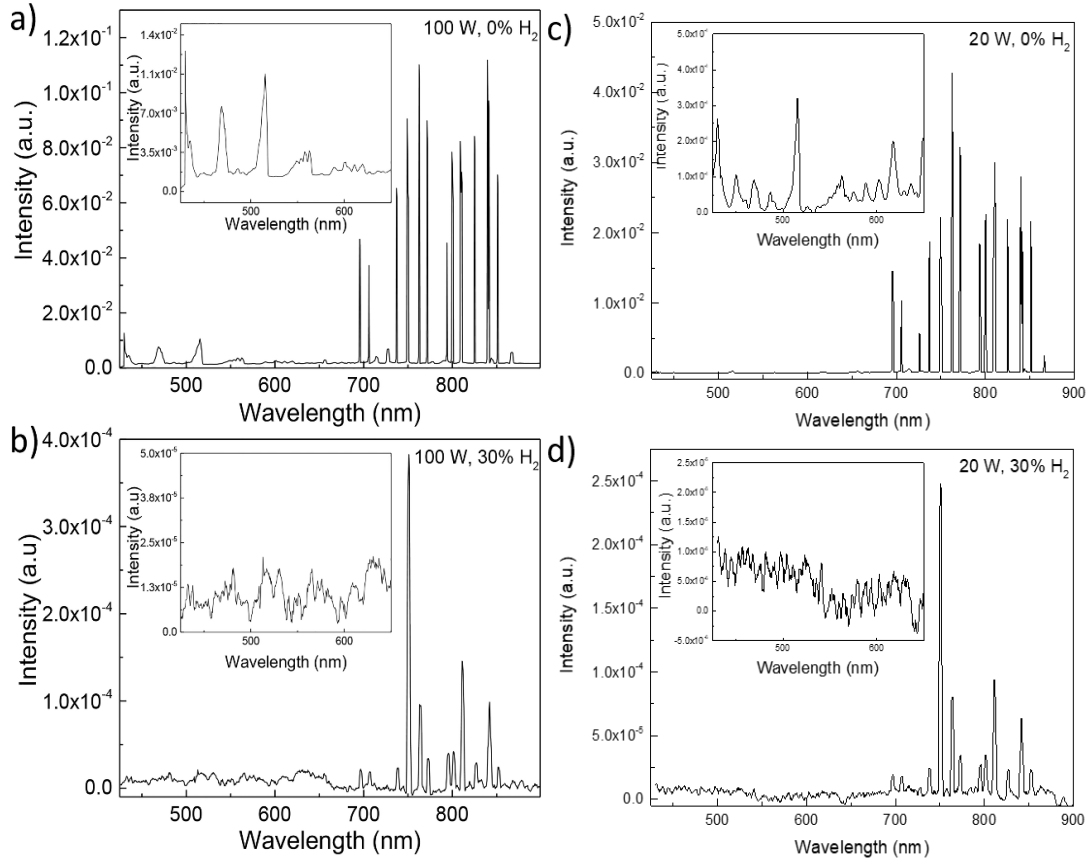
Figure 2.7. Optical emission spectra observed in a plasma produced at 20 and 100W; (a) and (c) are devoid of H_2, (b) and (d) are the H_2 rich environment. The insets show a higher magnification of the spectral region between 425 nm and 650 nm.

Finally, we would like to stress that nickel and other metallic particles have been

produced in atmospheric pressure microplasmas starting from metalorganic precursors.

While there is no reported data regarding the throughput and the precursor utilization rate

in such systems, the authors of these reports suggest that the particles are generated via a

homogeneous nucleation process and the particles are effectively carbon-free.[12a, 13, 19]

While understanding the details of particle nucleation is far from trivial, our results clearly suggest that nucleation and growth of nickel particles from nickelocene proceeds in a substantially different way in a low-pressure plasma system compared to the case of atmospheric pressure plasmas.

2.4 Conclusions

In this chapter, we have successfully demonstrated the use of a continuous flow, non-thermal discharge for the production of metallic nanoparticles. Although this system cannot produce entirely carbon-free Ni nanoparticles, we achieved substantial control of the synthesized nanomaterial properties in terms of chemical composition, size distribution and structure. Notably we have observed the formation of core-shell Ni-C structures, currently investigated by other groups as promising non-precious catalysts, and we believe that the reported mass yield can be increased after a careful optimization of the synthesis process. With regards to this first attempt at obtaining a monodisperse, pure, and conductive material that is necessary for this dissertation, we find this particular metallic nanoparticle synthesis endeavor insufficient for the reasons stated above; however further work into the ease of carbon nanoparticle synthesis as noted here using a continuous flow non-thermal reactor warrants merit as a potential candidate for dust injection as detailed in Chapter 1.

2.5 References

(1)   a) Schrick, B., J.L. Blough, A.D. Jones, and T.E. Mallouk, *Chemistry of Materials*. **14**, 140-5147 (2002); b) Roberts, E.J., S.E. Habas, L. Wang, D.A. Ruddy, E.A. White, F.G. Baddour, M.B. Griffin, J.A. Schaidle, N. Malmstadt, and R.L. Brutchey, *ACS Sustainable Chemistry & Engineering*. **5**, 632-639 (2017).

(2)   Pan, Y., R. Jia, J. Zhao, J. Liang, Y. Liu, and C. Liu, *Applied Surface Science*. **316**, 276-285 (2014).

(3)   Doria, G., J. Conde, B. Veigas, L. Giestas, C. Almeida, M. Assunção, J. Rosa, and P.V. Baptista, *Sensors*. **12**, 1657 (2012).

(4)   Krenn, J.R., A. Dereux, J.C. Weeber, E. Bourillot, Y. Lacroute, J.P. Goudonnet, G. Schider, W. Gotschy, A. Leitner, F.R. Aussenegg, and C. Girard, *Physical Review Letters*. **82**, 2590-2593 (1999).

(5)   a) Njoki, P.N., I.I.S. Lim, D. Mott, H.-Y. Park, B. Khan, S. Mishra, R. Sujakumar, J. Luo, and C.-J. Zhong, *The Journal of Physical Chemistry C*. **111**, 14664-14669 (2007); b) Pina, G., C. Louis, and M.A. Keane, *Physical Chemistry Chemical Physics*. **5**, 1924-1931 (2003); c) He, X., W. Zhong, C.-T. Au, and Y. Du, *Nanoscale Research Letters*. **8**, 446 (2013).

(6)   a) Kortshagen, U., *J. Phys. D: Appl. Phys.* **42**, 113001 1-22 (2009); b) Holman, Z.C. and U.R. Kortshagen, *Nanotechnology*. **21,** 2010; c) Nava, G., F. Fumagalli, S. Gambino, I. Farella, G. Dell'Erba, D. Beretta, G. Divitini, C. Ducati, M. Caironi, A. Cola, and F. Di Fonzo, *Journal of Materials Chemistry C*. **5**, 3725-3735 (2017).

(7)   Thimsen, E., M. Johnson, X. Zhang, A.J. Wagner, K.A. Mkhoyan, U.R. Kortshagen, and E.S. Aydil, *Nat Commun*. **5** (2014).

(8)   a) Coleman, D., T. Lopez, O. Yasar-Inceoglu, and L. Mangolini, *Journal of Applied Physics*. **117**, 193301 (2015); b) Alvarez Barragan, A., N.V. Ilawe, L. Zhong, B.M. Wong, and L. Mangolini, *The Journal of Physical Chemistry C*. **121**, 2316-2322 (2017).

(9)   Chaukulkar, R.P., K. de Peuter, P. Stradins, S. Pylypenko, J.P. Bell, Y. Yang, and S. Agarwal, *Acs Applied Materials & Interfaces*. (2014).

(10)   Lopez, T. and L. Mangolini, *Journal of Vacuum Science & Technology B*. **32**, 061802 (2014).

(11)   Yasar-Inceoglu, O., T. Lopez, E. Farshihagro, and L. Mangolini, *Nanotechnology*. **23**, 255604 (2012).

(12)   a) Chiang, W.-H., C. Richmonds, and R.M. Sankaran, *Plasma Sources Science and Technology*. **19**, 034011 (2010); b) Chiang, W.H. and R.M. Sankaran, *Journal of Physical Chemistry C*. **112**, 17920-17925 (2008).

(13)   Kumar, A., S. Kang, C. Larriba-Andaluz, H. Ouyang, C.J. Hogan, and R.M. Sankaran, *Nanotechnology*. **25**, 385601 (2014).

(14)   Torres-Gómez, L.A., G. Barreiro-Rodríguez, and F. Méndez-Ruíz, *Thermochimica Acta*. **124**, 179-183 (1988).

(15)   Lin, C.-Y. and R.C. Dunbar, *The Journal of Physical Chemistry*. **99**, 1754-1759 (1995)

(16)   a) Sheehan, M.K., M. Rudden, H. Cai, and C.-K. Tsung, *Catalysis Letters*. **146**, 309-318 (2016); b) Pisiewicz, S., D. Formenti , A.-E. Surkus, M.-M. Pohl, J. Radnik, K. Junge, C. Topf, S. Bachmann, M. Scalone, and M. Beller, *ChemCatChem*. **8**, 129-134 (2016).

(17)   Brissonneau, L., R. Sahnoun, C. Mijoule, and C. Vahlas, *Journal of the Electrochemical Society*. **147**, 1443-1448 (2000).

(18)   a) Rohlfing, E.A., *The Journal of Chemical Physics*, **1988**. 89(10): p. 6103-6112; b) Elliott, M.A., P.W. May, J. Petherbridge, S.M. Leeds, M.N.R. Ashfold, and W.N. Wang, *Diamond and Related Materials*. **9**, 311-316 (2000).

(19)   a) Lin, P.A. and R.M. Sankaran, *Angewandte Chemie*. **123**, 11145-11148 (2011); b) Lin, P.A., A. Kumar, and R.M. Sankaran, *Plasma Processes and Polymers*. **9**, 1184-1193 (2012).

Chapter 3: Graphitization of carbon particles in a non-thermal plasma reactor

3.1 Introduction

Non-thermal plasmas as nanoparticle synthesis tools offer many attractive characteristics, most notably for this work include: imparting a unipolar negative charge distribution on the particles due to the high flux of electrons compared to ions[1-3] which slows down agglomeration and enables the production of ultra-fine powders; confinement of the negatively charged particles within the plasma due to the presence of a built-in an electric field in the space charge sheath region[4,5]; intense heating of nanoparticles due to electron-ion recombination and other surface-driven reactions[6-9], leading to the ability of producing nanocrystals of high melting point materials such as silicon and titanium nitride[10,11]. Indeed, these attractive characteristics are of particular interest with respect to this dissertation—successfully designing a system to synthesize monodisperse, conductive nanoparticles with possible full consumption of the precursor molecule. Despite these promising reports, there are still significant gaps of knowledge in the processing science of nanoparticles - NPs - in plasmas. In particular, the plasma-driven heating mechanism that is usually considered responsible for the formation of high-quality nanocrystals is a complex phenomenon that has been difficult to probe experimentally. Few reports discuss the possibility of measuring the NPs temperature during the synthesis process through spectroscopic techniques. Lange et al. used optical emission spectroscopy to determine the self-absorption and calculate particle temperatures in a d.c. carbon arc discharge[12]. Fluorescent spectroscopy has been used on micron sized phosphorescent magnesium fluorogermanate nanoparticles suspended in a RF glow discharge, determining a particle

temperature of 410 K, 75 K above the gas temperature[13]. Stoffels et al. proposed the dominant NP cooling mechanism in the plasma environment to be blackbody radiation[14], which lends credence to the larger-than-ambient temperatures these particles seem to accrue. Indirect confirmation of nanoparticle heating in non-thermal continuous flow plasmas was discussed by Lopez[9,15] by monitoring the kinetics of crystallization of silicon particles and by measuring the desorption of hydrogen from the surface of silicon particles[16]. These last reports provide some confirmation both that the nanoparticle temperature can be quite high in these systems (>700K), and that these are difficult systems to probe experimentally. Here, we utilize some of the same experimental techniques described in[9,16], in particular with respect of in-situ, in-flight Fourier Transform Infrared Spectroscopy (FTIR), but this time focusing on carbon instead of silicon nanoparticles. The main advantage of this revised approach is the much larger absorption cross-section of carbon, which increases the sensitivity of the measurement. We have produced carbon particles using acetylene (C_2H_2) as a precursor and monitored the change in the FTIR spectrum with respect of the precursor consumption and of the various features related to CH_x bonding configurations. Moreover, we have observed the clear signature of Rayleigh scattering at low power, and emission from the system in the higher power regime. The high-power spectra can be well fit with a black body emission curve, suggesting that the particles exceed a temperature of 2000K in the discharge. In-situ Residual Gas Analyzer (RGA) measurements confirm the full consumption of C_2H_2 downstream of the plasma, and ex-situ characterization by Raman and Transmission Electron Microscopy (TEM) confirms that the high-power regime leads to the production of monodisperse graphitic

nanoparticles, satisfying the requirements outlined in Chapter 1 for a dust injection candidate.

3.2 Experimental Techniques

Figure 3.1 provides a schematic and a picture of the reactor design used in this work which comprises two quartz tubes (with outer diameter of 25.4 mm and inner diameter of 20 mm) intersected at 90° into a cross shape. An Ar:C2H2:H2 gas (65 sccm: 2 sccm:1.5 sccm) is flown along the longer arm of the system where a plasma discharge is maintained by a dual-copper ring electrode (spacing 5 cm) powered by an RF power supply (13.56MHz). The powered-electrode is connected to the RF generator through an L-type matching network that is used to eliminate reflected power. The power values reported in this work refer to the power output of the RF generator. While this is likely different than the actual power dissipated by the discharge, it is in our experience a reliable indicator from the point of view of reproducibility across different experimental runs and samples. Upon striking the RF discharge, the formation of highly energetic species gives way to the dissociation of C2H2 and enables the formation of carbon nanoparticles. The total pressure in the reactor is kept at 7.5 Torr by an automatically controlled butterfly valve placed downstream of the reactor. RF powers between 20 and 100W are used in this study.
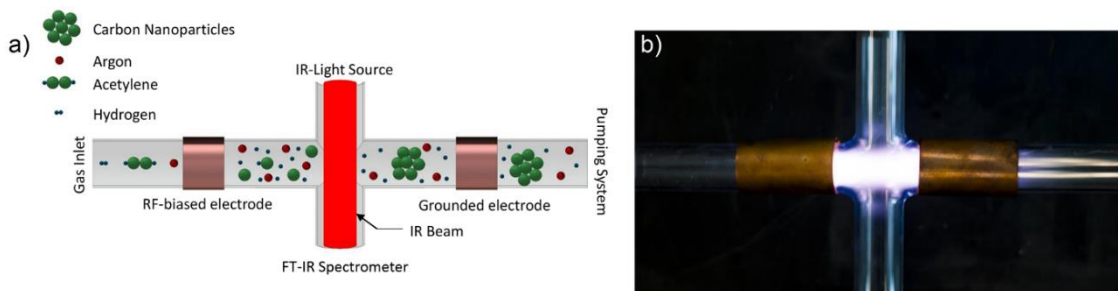
Figure 3.1. Schematic (a) and picture (b) of the system used for synthesis of carbon nanoparticles.

An IR-beam is sent through the length of the shorter quartz arm of the reactor and allows for in-flight measurement of Fourier Transform Infrared Spectrum of the gaseous precursor molecules and nucleated carbon nanomaterials. The FTIR measurements were performed using a Newport-Oriel modular FTIR system (MIR8035) with a SiC IR source, KBr beamsplitter, and a DTGS detector (all with a range of 350 cm^{-1} to 6000 cm^{-1}). The IR beam is sent perpendicularly through the plasma volume allowing for direct measurement of particle behavior inside the discharge. The acquisition scans are performed with a resolution of either 8 cm^{-1} (range 600 cm^{-1}- 4000 cm^{-1}) or 32 cm^{-1} (range 500 cm^{-1}- 6000 cm^{-1}) to measure the fine and broad features in the absorption spectra. The carbon nanoparticle production yield is measured for all the investigated RF power values. The carbon powder is collected on fine stainless-steel mesh for one hour and the mass of the deposit is obtained with Sartorius ENTRIS64-1S microbalance.

TEM imaging is carried out on a Tecnai12 microscope. Carbon NPs are collected on a copper TEM grid attached to a stainless-steel mesh filter located downstream of the plasma volume. A collection time of 5 seconds is used in all the investigated synthesis conditions. Particle size distributions (PSDs), average nanoparticle size and standard

deviation are derived from an ensemble of 100 NPs using ImageJ software. The Raman Spectra of the synthesized materials are recorded in the spectral range 800 cm^{-1}-3600 cm^{-1} using a micro Raman Horiba LabRam microscope (laser source wavelength 532 nm, laser power 0.06 mW, 50× objective). Samples are prepared by collecting a few milligrams of powder onto a filter placed downstream of the reactor, diluting the powder with chloroform, drop-casting the solution onto copper substrates and evaporating the solvent at room temperature.

3.3 Results and Discussion

We synthesize carbon nanoparticles according to the processing conditions outlined in the experimental section and investigate the dependence of the characteristics of the synthesized material on the RF input power level (20 W- 100W). Figure 3.2 summarizes the carbon nanoparticles properties on the two outer extremes of the described RF power parameter space. At 20 W, the TEM micrograph highlights the nucleation of purely amorphous spherical carbon nanoparticles (see Figure 3.2a). Further strengthening the TEM analysis, the corresponding Raman spectrum displays a large photoluminescence background and the lack of distinct first-order peaks, compatible with a highly hydrogenated amorphous carbon – a-C:H – material (see Figure 3.2b)[17]. As the input RF power is increased to 100W, a transition from an amorphous to a highly-graphitic carbonaceous material– grC - is observed. The TEM micrograph shows well defined collapsed graphene-like layers (see Figure 3.2d), while sharp D and G peaks and pronounced second order features (D', D'' and 2D' peaks) emerge in the corresponding

33

Raman spectrum endorsing the high degree of crystallinity of the material (see Figure 3.2e)[18]. The lack of a photoluminescence background indicates, on the other hand, a low degree of hydrogenation[17]. For both conditions, the PSD is relatively monodisperse (see Figure 3.2c and Figure 3.2f). Interestingly, the particles produced at higher power are smaller, with an average diameter of 12 nm (±4 nm) at 20 W and 6 nm (±2 nm) at 100 W. Although we have not specifically focused on the influence of process parameters on size distributions, we hypothesize that a higher power will lead to a faster nucleation rate and to the formation of smaller particulate.
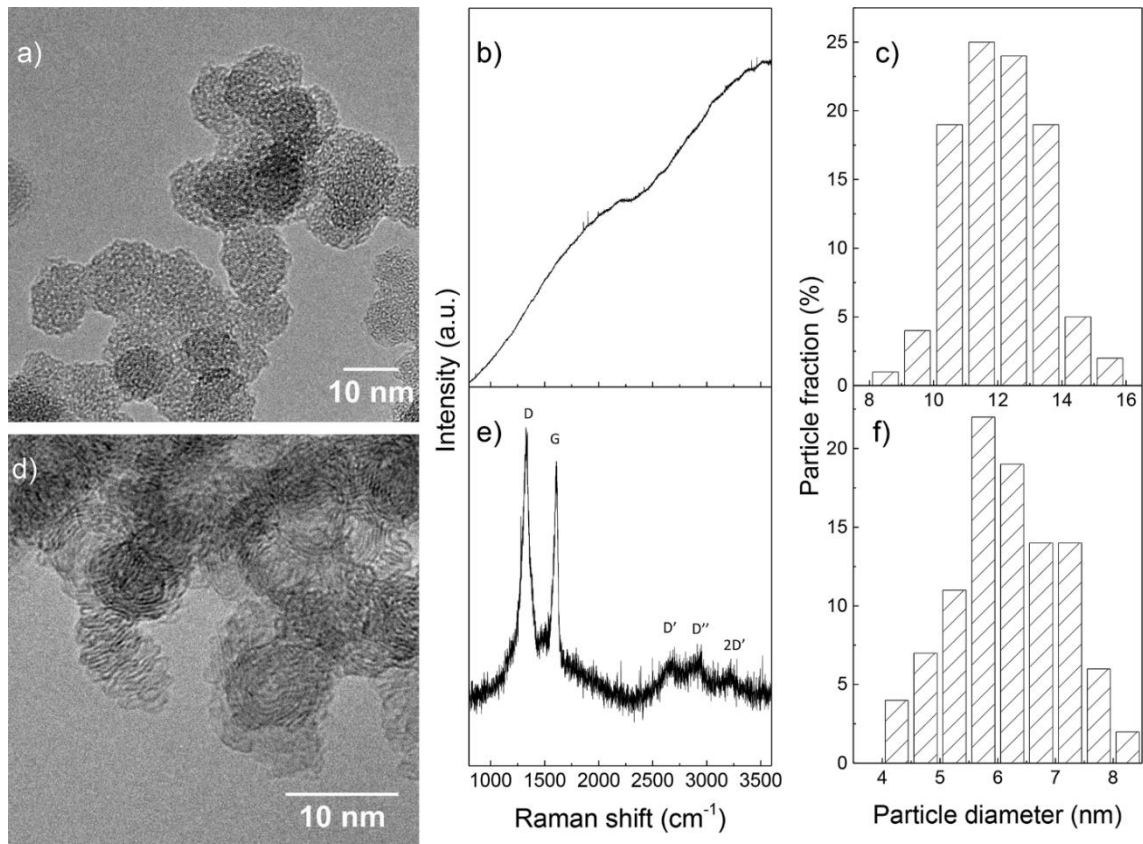
Figure 3.2. TEM micrographs of carbon nanomaterials synthesized below (a) and above (d) the power threshold for material graphitization, 20 W and 100 W respectively. (b) and (e) show the Raman spectra of the materials of (a) and (b). The PSD of the materials of (a) and (b) is depicted in figures (c) and (f).

To better elucidate the transition from the "aC:H" to the "grC" region, we acquired a series of Raman measurements from 20 W to 100 W RF power in steps of 20 W (the corresponding spectra are reported in Figures 3.3 and 3.4). A sharp changeover from "aC:H" to "grC", corresponding to the onset of the nanoparticle crystallization in the plasma phase, is observed above 40 W with the appearance of a G peak around 1610 cm^{-1} and D peak around 1330 cm^{-1}. The position of the G peak, higher with respect to the values typically reported for amorphous carbon (around 1510 cm^{-1}), points at the presence of a substantial amount of nanographite in the synthesized material.
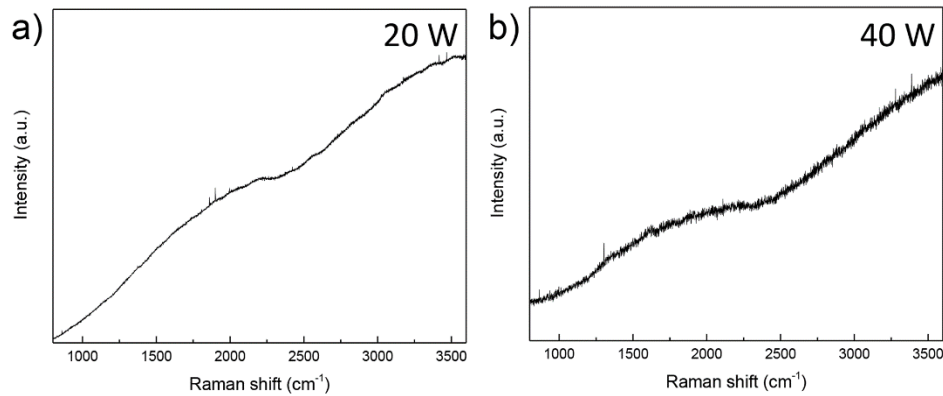
Figure 3.3. Raman spectra of carbon nanomaterials synthesized for increasing values of RF power in the "a-C:H region."
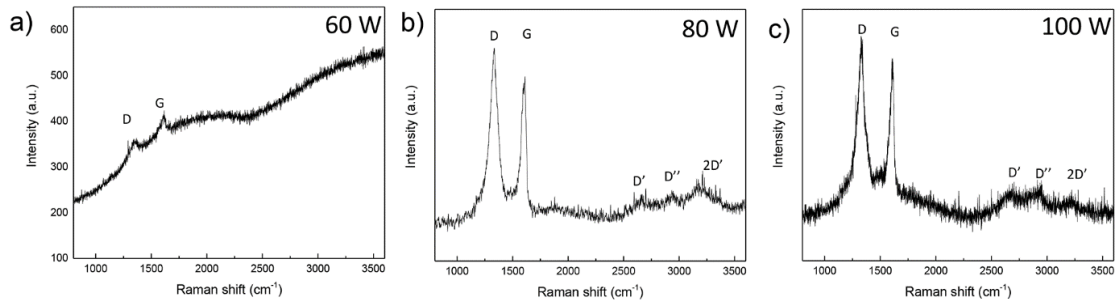
Figure 3.4. Raman spectra of carbon nanomaterials synthesized for increasing values of RF power in the "Graphitic C region."

In order to gain insight into the variation of the structural properties in the "grC region", we performed a spectral de-convolution of the measured Raman signals in the 1100 cm^{-1}- 1800 cm^{-1} spectral range. The fitting routine encompasses a Lorentzian peak for the D component, a Breit-Wigner-Fano -BWF- line-shape for the G component and a linear baseline to account for the photoluminescence superimposed to the Raman spectrum (see Figure 3)[17], [19], [20]. The intensity ratio of the D and G peaks - ${I_D}/{I_G}$ - constitutes a metric related to the material degree of graphitization. The slope of the linear photoluminesce background normalized to the intensity of the G peak - ${I_D}/{I_G}$ - is, on the other hand, proportional to the amount of hydrogenation of the carbon nanoparticles[17,19].
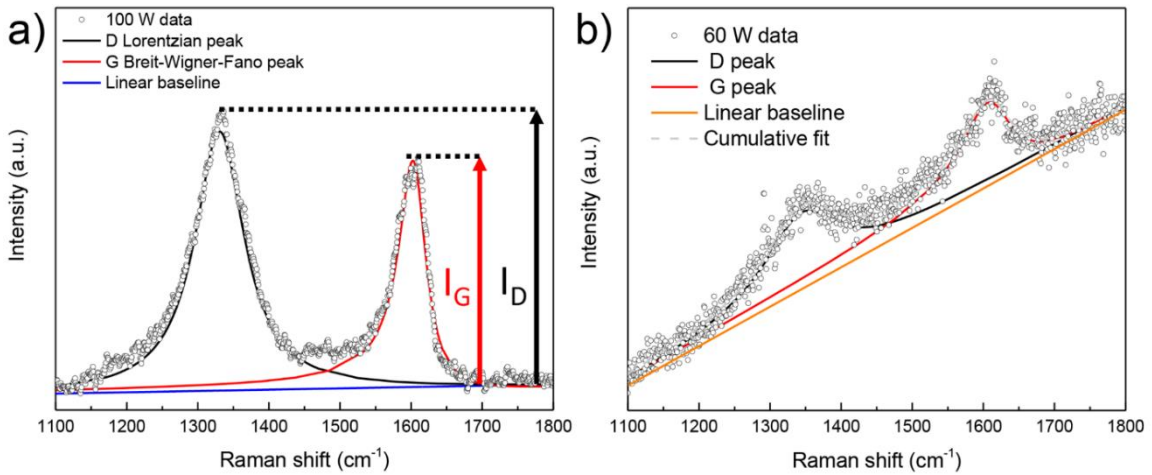
Figure 3.5. Raman spectrum of the carbon nanomaterials synthesized at 100W in the "grC" region (a). The graph displays an example of the Raman spectrum fitting scheme comprising a Lorentzian peak for the D component, a BWF line-shape for the G component and a linear baseline. I_D and I_G represent the intensity of the D and G peaks respectively. (b) shows the multi-peak fittings of the Raman spectra for the carbon nanomaterials synthesized in the "grC region" at the 60W condition.

Increasing the RF power from 60 W to 100 W, we observe a rapid enhancement of the material graphitization which is marked by the increase of the value of ${I_D}/{I_G}$ from 0.85

at 60 W to 1.15 at 80 W -100 W, well above the values typically reported in the literature for amorphous carbon, and a substantial loss of bonded hydrogen, which is highlighted by the decrease of m/I_G from 40 at 20 W to 0.5 at 80 W-100 W (see Figure 3.6). The decrease of the G peak FWHM from 40 cm^{-1} at 20 W to 20 cm^{-1} at 80 W -100 W highlights also a reduction in the structural disorder, namely C-C bond length and bond angle distortion. We observe a stark correlation between the mechanism for graphitization and the decreasing hydrogenation. The intense and well-known plasma-induced nanoparticle heating likely brings the nanoparticles above the graphitization threshold temperature inducing at the same time the thermal effusion of hydrogen from the nucleated material. The observed phenomenology is hence similar to the experimental observations reported in previous works for silicon-forming non-thermal plasmas[7,21]. The incandescence measurements, described later in this manuscript, support this conclusion.
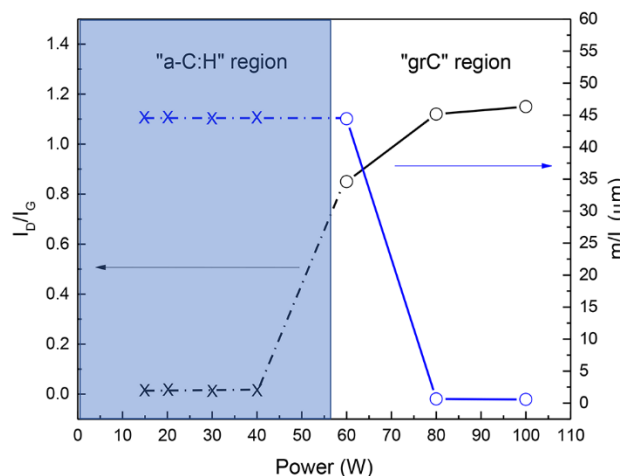
Figure 3.6. A mapping of the ${}^{I_D}/_{I_G}$ and ${}^{m}/_{I_G}$ ratios as a function of the RF power coupled into the plasma discharge. As the a-C:H region shows no quantifiable D or G peaks, the corresponding values could not be derived and are indicated with an 'x' (${}^{I_D}/_{I_G}$ is set to zero to highlight the purely amorphous nature of the material, while ${}^{m}/_{I_G}$ is maintained at the same value measured at 60 W, assuming a hydrogenation likely equal or higher to this condition).

To further elucidate the synthesis process dependence on the plasma power and the associated plasma heating mechanism, we performed an in-situ FTIR spectroscopic investigation during the nanoparticle nucleation in the plasma reactor for increasing RF power levels. The reference spectrum of the employed gas mix and the two extremes of the "a-C:" and "grC" regions, 20 W and 100 W respectively, are depicted in Figure 3.7. The spectrum of the Ar:C2H2:H2 gas mix in the "plasma off" condition shows the IR active signatures of the precursor molecule (see Figure 3.7) that we identified from the Coblentz Society's IR spectra collection and NIST ChemWebBook, i.e. 729 cm⁻¹, 1300 and 1350 cm⁻¹, 2334 and 2361 cm⁻¹, and 3250-3310 cm⁻¹.
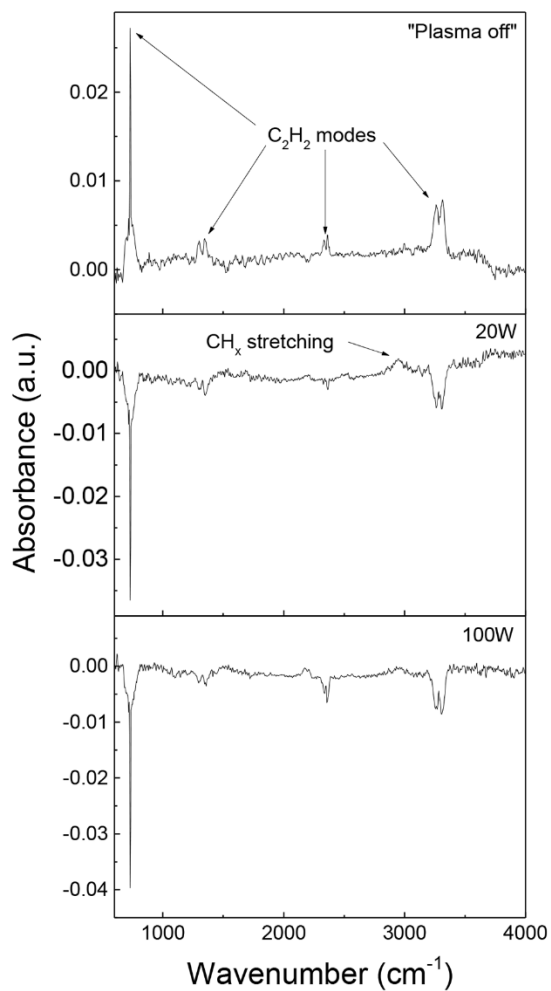
Figure 3.7. In-situ FTIR spectra collected for the $Ar:C_2H_2:H_2$ gas mix in "plasma-off" condition, at 20 W and 100W RF input power. The signals were collected at 8 cm^{-1} resolution.

The "plasma on" spectra are obtained using the "plasma off" condition as a reference, without changing the gas composition (i.e. with the acetylene still flowing). For this reason, the acetylene modes appear as negative on an absorbance scale, suggesting that acetylene is consumed when the plasma is ignited. The absolute intensity of the acetylene peaks in the 20 W and 80 W scans is very close to that in the "plasma off" spectrum, suggesting an almost complete depletion of the C2H2 precursor in the discharge volume across all RF input powers. Residual gas analyzer (RGA) measurements performed by sampling the gas composition downstream of the plasma confirm the full consumption of acetylene, as seen in Figure 3.8.
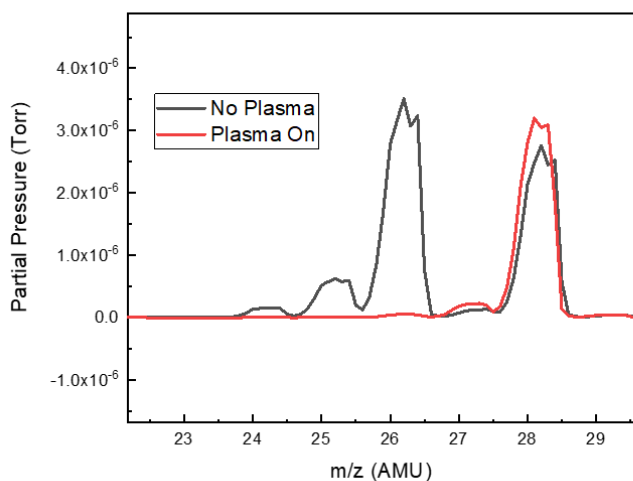
Figure 3.8. RGA measurements confirming the full consumption of C_2H_2, indicated by the absence of the 24, 25, and 26 AMU peaks under the "plasma on" condition.

The shoulder between 1660 and 1730 cm^{-1}, related to both C=C and C=O stretching, and the peaks around at 2180 and 2280 cm^{-1}, attributed to CO, are most probably due to the presence of residual oxygen and/or moisture in the system, while the shoulder around 1500

cm[-1] can be attributed to aromatic C=C stretching[22]. The broad shoulder around 2850-3100 cm^{-1} is attributed to the IR-active CH_x stretching modes of the carbon nanoparticles nucleating in the plasma discharge[23]. The integration of the area underlying the CH_x stretching mode, which is proportional to the hydrogenation of the synthesized carbon materials, corroborates the previous trend obtained from the fitting of the Raman spectra and shows progressive hydrogen thermal-driven loss at high RF powers (see Figure 3.9) in the processing parameter region corresponding to the formation of highly-graphitic nanomaterials. Notably, the spectrum acquired at 20W appears to exhibit a broad baseline which increases towards positive values at high wavenumbers.
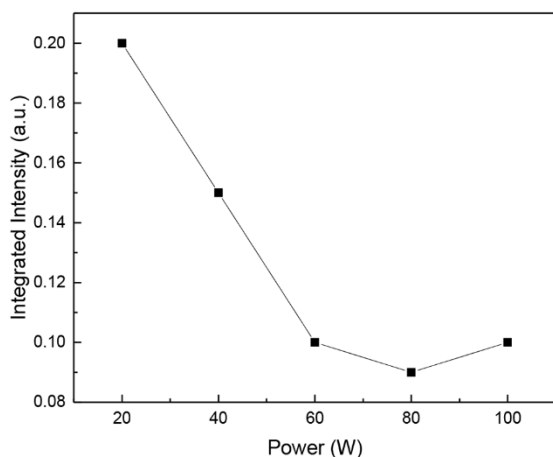
Figure 3.9. Integrated intensity of the CH_x shoulder at 2800-3100 cm^{-1} as a function on input RF power.

To further investigate this, we have acquired a second set of FTIR spectra as a function of the RF power on a broader spectral range (up to 6000 cm^{-1}) employing a lower resolution of 32 cm^{-1}. The use of a lower resolution decreases the acquisition time to roughly 3 minutes per scan (each scan is averaged 500 times), which we have found to be crucial to reproducibly investigate broadband changes in the absorption signal.
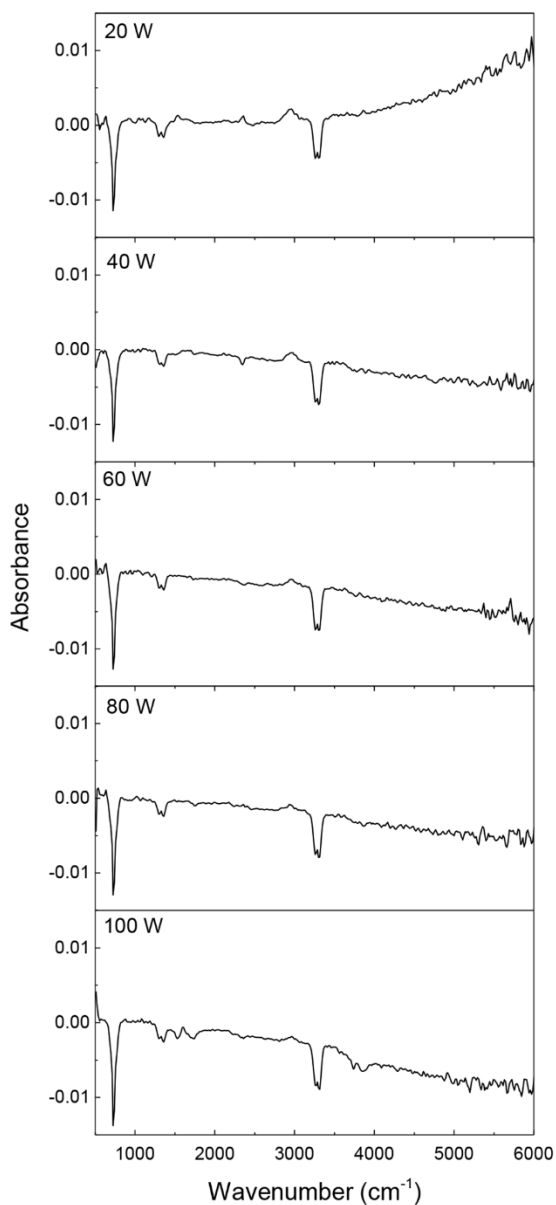
Figure 3.10. In situ FT-IR spectra as a function of the applied RF input power. The signals were collected at 32 cm^{-1} resolution.

Fluctuations in the IR source emission intensity, which manifest as broadband variation in the baseline signal and thus make the interpretation of the spectra troublesome, are unavoidable but in our experience their influence can be minimized by performing faster measurements. The results summarized in Figure 3.10 highlight a marked change of

the high-wavenumber behavior of the measured signal, which goes from positive values to negative ones upon increase of the RF power. The low RF power extreme of the parameter space, where negligible plasma-induced heating occurs and completely amorphous nanomaterials are produced, exhibits a behavior indicative of light scattering. On the other hand, the large negative signal for the higher power conditions is consistent with increased emission from the system. We attribute this signal to incandescence from the nanoparticles. This interpretation is consistent with the ex-situ material characterization, which suggests that particles are sufficiently hot to lead to graphitization of a-C:H[15]. To confirm that this signal originates from the particles and not from the plasma itself, we have performed absorbance measurement without acetylene and particles; for the same RF input power level we could not observe the same broadband emission from the system.

The FTIR spectrum measured on the extreme of the a-C:H region is fit with a Rayleigh scattering model, given the small size of the synthesized nanoparticles (Rayleigh criteria: $d_{particle} < \frac{1}{5}\lambda$), whereas for the high RF power condition we employed a "small-particle approximation" of the Planck's black-body radiation law, with respective equations detailed in (1) and (2). In relation to the black-body emission, due to the small particle size, an approximation is needed. Small-cluster emission is related to black-body emission through wavelength-dependent emissivity[24], which for microscopic bodies, is equal to the absorption efficiency - Q_{abs}. Q_{abs} exhibits a λ^{-1} dependence, which is directly equivalent to the wavenumber - v. The Beer-Lambert Law relating intensity to absorbance was used to properly fit the spectra.

$$\text{Rayleigh scattering: } A = -\log\left(1 + c_1(2\pi v^4)\left(\frac{d}{2}\right)^6 \left(\frac{n^2-1}{n^2+2}\right)^2\right) \tag{1}$$

$$\text{Black} - \text{Body Emission: } A = -\log\left(1 + \frac{c_2\, d\, v^4}{e^{\frac{h\, c\, v}{k_b T}}-1}\, Im\left(\frac{n^2-1}{n^2+2}\right)\right) \tag{2}$$

v being the wavenumber, d the particle diameter, h the Planck's constant, c the speed of light, k_b the Boltzmann constant, T the particle temperature and c_1 and c_2 the fitting parameters. Figure 3.12 summarizes the results of the FTIR spectral deconvolution. At 20 W the signal is well fitted by the employed Rayleigh scattering model as the particles are not at high enough temperature to exhibit sufficient black-body emission. We should stress that the nanoparticle density is not the same for different power inputs. Figure 3.11 shows a much higher particle production rate at lower power (corresponding to the amorphous particles) compared to the high-power case (corresponding to the graphitic particles). When normalizing over the acetylene mass flow rate, we calculate that the precursor-to-nanoparticle conversion rate is ~33% at a power input of 20W and ~10% at a power input of 100W. As already mentioned earlier, both the FTIR and RGA data confirm that acetylene is fully consumed for any of the power inputs discussed in this work. The reduction in nanoparticle production rate qualitatively correlates with the fact that we observe rapid growth of a carbon film on the inside walls of the reactor under high input power conditions.
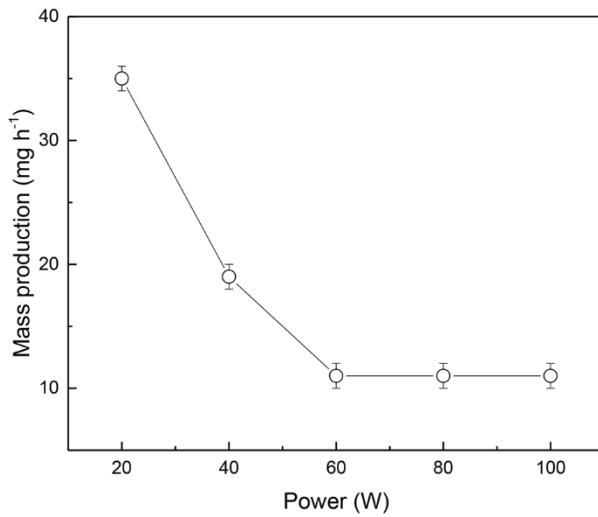
Figure 3.11. Variation of the absolute mass production yield as a function of RF input power.
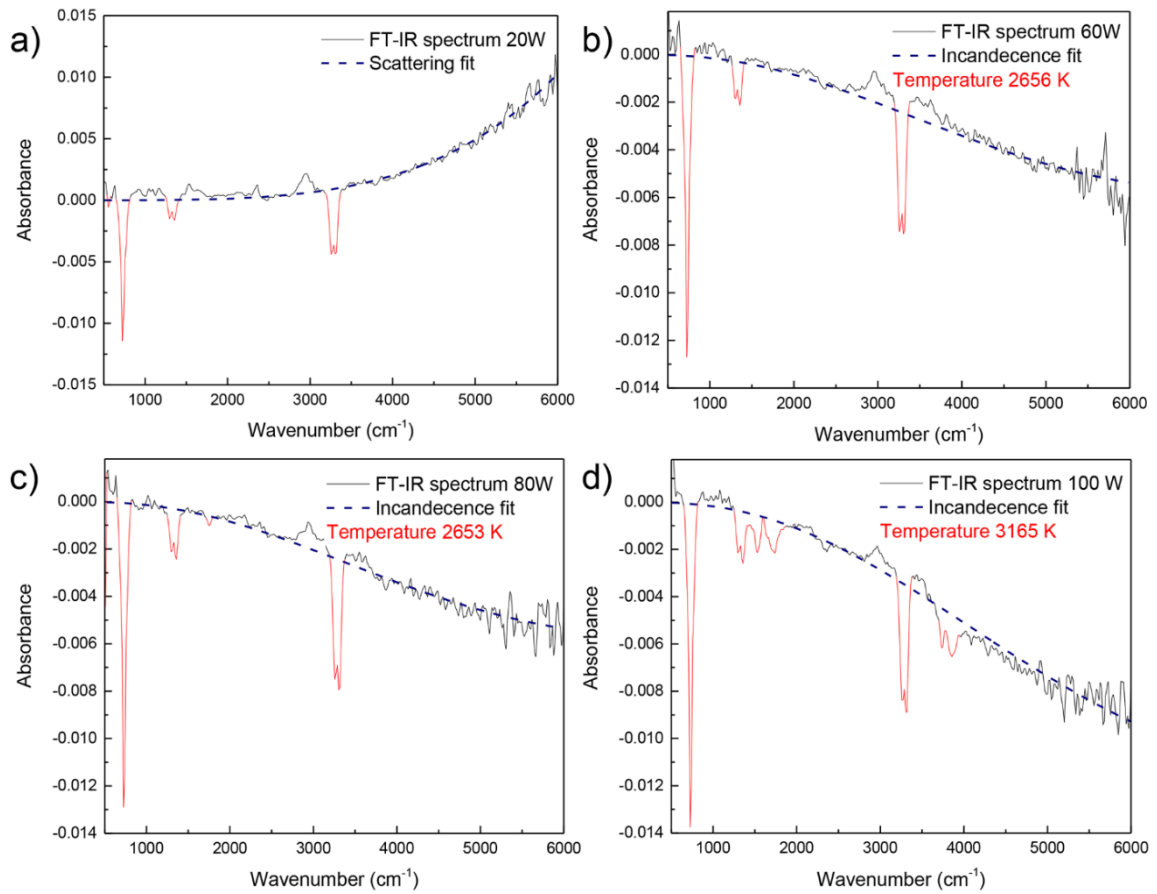
Figure 3.12. In situ FT-IR spectra measured at 20 W (a), 60 W (b), 80 W (c) and 100 W (d) RF input power. The data are fitted with a Rayleigh scattering model and a Black-Body emission model where appropriate. The NP temperature obtained from the Black-Body fit are reported in the corresponding graphs. The precursor gas FTIR modes are masked to increase the accuracy of the fitting procedure and are highlighted in red in the graphs.

Figure 3.12b, 3.12c, and 3.12d detail the black-body emission attributed to incandescence of the graphitic C particles. Although we cannot completely rule out the presence of scattering in the high RF power regime, we consider this, as a first approximation, to be negligible with respect to the particle incandescence. This assumption is motivated by the following considerations. Qualitatively, the significant particle size reduction observed at 100 W RF input power results in more than 60-fold downscaling of the scattering signal intensity with respect to 20 W. Additionally, the reduction of the mass yield for increasing powers (by a factor of 5 from 20W to 100W) also supports the conclusion that the contribution to the absorbance spectrum due to scattering is likely much smaller at 100W than for the 20W case. The influence of the variation of refractive index caused by the transition from "a-C:H" to "grC" results in a more moderate effect[25-27]. By fitting the shape of the broad feature in the absorbance scans with equation (2), we find that the particles approach temperature well above 2000K in the "grC" region. Previous literature reports that the graphitization of amorphous carbon black requires temperatures exceeding 2000K for several hours in vacuum[28] or temperatures ranging from 800-1500K at extremely high pressures for few minutes[29]. Other work on laser-induced crystallization of a-C at atmospheric pressure reports carbon crystallization temperatures comparable to the one reported in our investigation upon significantly reducing the timescale of the thermal process (around 8-100 ns)[30]. Further researchers have studied the graphitization

46

of particles on the same size scale as those produced in this work, reporting temperatures of 1000K over 6 hours[31]. In contrast, the particles synthesized in this work reside in the plasma volume for around 500 milliseconds and the system operates at 7.5 Torr, suggesting that it is reasonable to expect very high temperature, such as the ones obtained by fitting the black-body emission curve, to achieve complete graphitization.

3.4 Conclusion

Carbon nanoparticles have been synthesized in low-pressure non-thermal plasma discharge investigating the effect of different power level values on the synthesized material properties. The degree of graphitization and comparative hydrogenation have been studied through intensive Raman Spectroscopy; TEM imaging provided insight into the morphology and PSD of the extremes of the two reported synthesis regions; RGA measurements confirmed that, even at the lowest power level investigated, the C_2H_2 was fully consumed. To investigate the phenomenon behind the increasing degree of graphitization and decreasing hydrogenation levels, in-flight FTIR was used. Rayleigh scattering was observed at the extreme of the a-C:H region, attributed to low overall particle temperature and high production of nanoparticles. In the graphitic C region, particle incandescence was observed and fit to black-body emission behavior, with resultant fitting suggesting particle temperatures above 2000K. The high estimated particle temperature in this region invites the hypothesis of a correlation between both the crystallization of the a-C:H and the morphological transformation observed. Finally, the method outlined in this chapter is sufficiently modular to act as an addendum to any

Langmuir Probe-enabled system, delivering independently synthesized monodisperse, pure, and conductive nanoparticles to enable a simpler and more forgiving environment in which to investigate the effect of dust on plasma characteristics.

3.5 References

(1)   Goree, J., *Plasma Sources Sci. Technol.* **3**, 400–406 (1994).

(2)   Matsoukas T and Russell, M., *J. Appl. Phys.* **77**, 4285–4292 (1995).

(3)   Schweigert V. A. and Schweigert V. I.*, J. Phys. D. Appl. Phys.* **29**, 655–659 (1996).

(4)   Carlile, R.N., Geha, S., O'Hanlon, J. F., and Stewart, J. C., *Appl. Phys. Lett.* **59**, 1167–1169 (1991).

(5)   Selwyn, G. S., Heidenreich, J. E., and Haller, K. L., *Appl. Phys. Lett.* **57**, 1876–1878 (1990).

(6)   Bapat, A., Anderson, C., Perrey, C. R., Carter, C. B., Campbell, S. A., and Kortshagen, U. R., *Plasma Phys. Control. Fusion*. **46**, B97–B109 (2004).

(7)   Kramer, N. J., Anthony, R. J., Mamunuru, M., Aydil, E. S., and Kortshagen, U. R., *J. Phys. D. Appl. Phys.* **47**, 75202 (2014).

(8)   Mangolini, L. and Kortshagen, U., *Phys. Rev. E - Stat. Nonlinear, Soft Matter Phys.* **79**, 1–8 (2009).

(9)   Lopez, T. and Mangolini, L., *J. Vac. Sci. Technol. B, Nanotechnol. Microelectron. Mater. Process. Meas. Phenom.* **61802** (2014).

(10)   Barragan, A. A., Ilawe, N. V., Zhong, L., Wong, B. M., and Mangolini, L., *J. Phys. Chem. C*. **121**, 2316–2322 (2017).

(11)   Mangolini, L., Thimsen, E., and Kortshagen, U., *Nano Lett.* **5**, 655–659 (2005).

(12)   Lange, H., Saidane, K., Razafinimanana, M., Gleizes, A., *J. Phys. D. Appl. Phys.* **32**, 1024–1030 (1999).

(13)   Daugherty, J. E., *J. Vac. Sci. Technol. A Vacuum, Surfaces, Film.* **11**, 1126 (1993).

(14)   Stoffels, E., Stoffels, W. W., Kersten, H., Swinkels, G., and Kroesen, G. M. W., *Phys. Scr.* **89**, 168–172 (2001).

(15)   Lopez, T. and Mangolini, L., *Nanoscale*. **6**, 1286–1294 (2014).

(16)   Lopez, T. and Mangolini, L., *J. Vac. Sci. Technol. B, Nanotechnol. Microelectron.*

Mater. Process. Meas. Phenom. **34**, 41206 (2016).

(17)   Casiraghi, C., Ferrari, A. C., and Robertson, J., *Phys. Rev. B - Condens. Matter Mater. Phys.* **72**, 1–14 (2005).

(18)   Lee, Y. J., *J. Nucl. Mater.* **325**, 174–179 (2004).

(19)   Tai, F. C., Lee, S. C., Chen, J., Wei, C., and Chang, S. H., *J. Raman Spectrosc.* **40**, no. 8, 1055–1059 (2009).

(20)   Ferrari, A. C., and Robertson, J., *Phys. Rev. B*. **61**, 14095–14107 (2000).

(21)   Nava, G., et al., *J. Mater. Chem. C*. **5**, 3725–3735 (2017).

(22)   Kovačević, E., Stefanović, I., Berndt, J., and Winter, J., *J. Appl. Phys.* **93**, 2924–2930 (2003).

(23)   AllaMandola, A. G. G. M. T. L. J., and Sandford, S. A., *Astrophys. J.* 134–146, (1992).

(24)   Stoffels, W. W., Stoffels, E., Kroesen, G. M. W., and de Hoog, F. J., *J. Vac. Sci. Technol. A Vacuum, Surfaces, Film.* **14**, 588 (1996).

(25)   Duley, W. W., *Astrophys. J.* 694–696 (1984).

(26)   Zubko, E. B. V. G., Mennella, V., Colangeli, L., *Mon. Not. R. Astron. Soc.* **4**, 1321–1329 (1996).

(27)   Son, S., Taheri, M., Carpenter, E., Harris, V. G., and McHenry, M. E., *J. Appl. Phys.* **91**, 7589–7591 (2002).

(28)   Houska, C. R., and Warren, B. E., *J. Appl. Phys.* **25**, 1503–1509 (1954).

(29)   Onodera, A., Irie, Y., Higashi, K., Umemura, J., and Takenaka, T., *J. Appl. Phys.* **69**, 2611–2617 (1991).

(30)   Abrahamson, J. P., **124**, 6–8 (2017).

(31)   Barbera, K., *et al.*, *Chinese J. Catal.* **35**, 869–876 (2014).

Chapter 4: Langmuir probe characterization of an Ar-H$_2$ non-thermal plasma loaded with carbon nanoparticles

4.1 Introduction

Low-temperature gas discharges are widely employed in several industrial manufacturing processes, such as thin-film deposition, material functionalization and etching. The formation of particles represents an ever-present issue in processing plasmas, and the investigation of particle-related phenomena led to the genesis of what we call "science of dusty-plasmas". The formation of particulate in a plasma discharge, at first regarded merely as problem to be tackled[1,2], has been later investigated as a possible route for the controlled fabrication of nanopowders. Non-thermal plasma processes have been successfully optimized for the deliberate formation of nanoparticles, as confirmed by several reports on the non-thermal plasma synthesis of high quality nanocrystals composed of a broad range of materials[3,4]. These methods are attracting a growing interest, possibly representing a key enabler for the future large-scale utilization of various nanoarchitectures in plasmonic[5,6], thermoelectrics[7], microelectronics[8-10] and energy-storage applications[11-13]. Unveiling the fundamental physics and properties of dusty discharges clearly represents a crucial requirement to gain a better understanding of all the aforementioned plasma-based systems and contribute to their engineering and optimization. Among several plasma characterization techniques, the Langmuir probe method represents one of the most established measurement routines.

The in-depth analysis of the probe current-voltage characteristics provides detailed information regarding the ion and electron densities, the electron temperature and the electron energy distribution function[14,15]. The method has been widely adopted across industrial plasmas for the real-time monitoring of the plasma characteristics and the tuning of the operating conditions. In dust-forming plasmas, however, the application of the Langmuir probe measurement remains a challenging endeavor. The growth of insulating films over the probe surface severely affects the reliability of the measurement. The successful application of the Langmuir probe method in a dusty plasma requires substantial modifications of the probe design and elaborate measurement strategies to tackle issues related to particle formation. For instance, Bilik et al.[16] have developed a shielded Langmuir probe technique to measure the EEDF in a low-pressure silane-containing plasma, and successfully monitored its evolution during the nucleation and growth of silicon particles. In this study, the probe is isolated from the plasma via a retractable ceramic shield during most of the process and exposed to the plasma only during brief periods of time to perform the I-V measurement. This ingenious, while non-trivial, approach is therefore applied to the complex scenario in which the precursor is continuously supplied to the plasma volume in which the probe is inserted, with particle nucleation and growth, together with growth of a thin film via CVD, also continuously occurring.

In this chapter, we present a simpler approach based on a standard Langmuir probe measurement to successfully investigate the relation between plasma properties and the introduction of nanoparticles into a non-thermal low-pressure discharge. A radio frequency

(RF) argon-hydrogen - Ar-H$_2$ - plasma is generated in a primary reactor with a planar-coil inductive source. The reactor is controllably dosed with conductive graphitic carbon nanoparticles produced in a secondary RF Ar-H$_2$ plasma from the dissociation of acetylene - C$_2$H$_2$. This allows decoupling the particle nucleation phase from the plasma in which the measurement is performed, since the precursor is fully converted into nanoparticles in the nanoparticle-producing plasma. As a consequence, this approach offers a pathway towards investigating the effect of common process parameters, such as pressure, gas composition, electrical input power, on a dusty plasma which is controllably and consistently dosed with the same particles, in terms of their composition, size and density. We have found that the use of graphitic nanoparticles, in combination with the elimination of the CVD film growth on the probe tip (the precursor is fully consumed in the nanoparticle-producing step), allows for a measurement environment that is substantially more forgiving to the Langmuir probe technique. No changes were observed in the EEDF measured for a pristine plasma before and after several measurements performed in the dusty plasma regime. For this study, we focus on the effect of primary plasma RF power on plasma properties in the dust-rich conditions. As expected from theory and previous literature, nanoparticles act as electron sinks, reducing the electron density inside the plasma volume and severely affecting the power coupling. Notably, contrary to theory, an increase in the electron temperature value was observed upon increase of the primary power-input to the plasma in dust-rich conditions. The number of charges per nanoparticle is derived across the space of the investigated plasma parameters by monitoring the deficit between ion and electron

densities. The particle charge has been found not to increase monotonically with plasma density. It decreases for high input plasma power.

4.2 Experimental Techniques

Figure 4.1(a) depicts the system used in the experiments. The primary reactor consists of a cylindrical stainless-steel vacuum chamber covered by a circular alumina plate (diameter 32 cm and thickness 1 cm) with a grounded Faraday shield and connected to a Leybold TURBOVAC SL80 turbopump. The Ar-H_2 is produced in the primary chamber with a three-turn planar coil. The secondary reactor - nanoparticle production cell - comprises a 2.54 cm diameter quartz tube reactor with a copper ring electrode and a grounded 2 mm orifice. The system is designed to inject the produced particles in the center of the primary plasma. The gas mixture supplied through the nanoparticle production cell comprises of 28 sccm of Ar, 0.6 sccm of H_2 and 0.28 sccm of acetylene (C_2H_2).
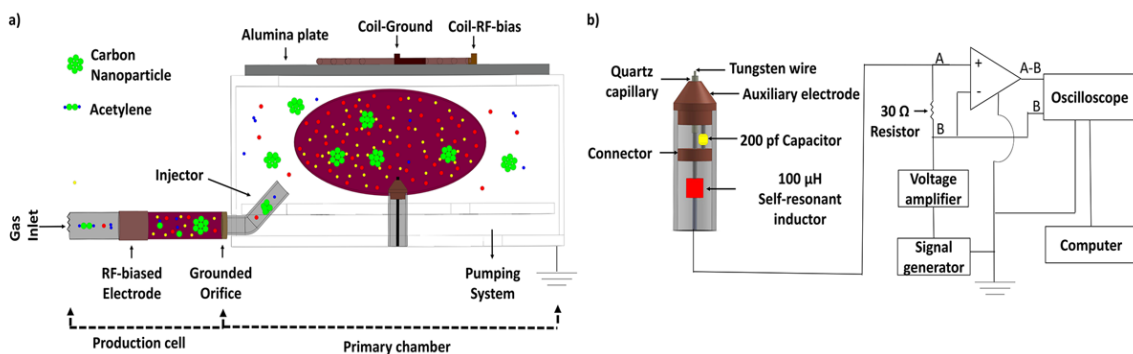
Figure 4.1. a) Schematic of the system showing nanoparticle production cell, nanoparticle injection system and the primary chamber. b) Schematic of the probe design and measurement system.

We have performed extensive residual gas analyser (RGA) measurements confirming that the nanoparticle precursor (acetylene) is fully converted to nanoparticles

during the nanoparticle production step. The RF power supplied to the first plasma is 70 W. The pressure in the nanoparticle-producing plasma is 2.3 Torr, while the pressure in the primary chamber is 150 mTorr. The mass production rate of the carbon nanoparticles was determined by collecting the synthesized material on stainless-steel mesh for 2 h and measuring the mass of the deposit with a Sartorius ENTRIS64-1S microbalance. TEM analysis was performed on the synthesized material on a Tecnai12. The particle size distribution, the average nanoparticle size and the standard deviation were obtained from the measurement of an ensemble of 100 nanoparticles using ImageJ software. The Raman spectrum of the carbon nanoparticles was acquired with a Raman Horiba LabRam microscope (spectral range 400–4000 cm^{-1}, laser wavelength 532 nm, laser power 0.06 mW, objective 50×). The powered-electrodes of the primary and secondary reactors are connected to independently controlled RF generators through an L-type matching network. In this work, the power values reported for the primary plasma refer to the actual power coupled into the discharge which is calculated with the following procedure:

1. The desired gas mixture is flowed into the primary reactor and the desired RF power is supplied while tuning the matching network to minimize reflected power.

2. The net power (forward minus reflected), and the RMS current through the planar-coil, which is measured with a Pearson 2877 current probe, are recorded.

3. The system is evacuated at its base pressure, typically around 10^{-6} Torr

4. The RF power is again supplied to the reactor without striking a discharge. Power is adjusted to match the RMS current measured in point 2. The new net power (forward

minus reflected) is recorded. This value represents the losses due to joule heating and radiation through the coil and the matching network.

5. The actual power is calculated as the difference between the net powers measured in point 2 and point 4.

Figure 4.1(b) depicts Langmuir probe and the measurement system employed for the acquisition of the I-V characteristics. The Langmuir probe is positioned in the center of the primary reactor along a line perpendicular to the plane of the coil. The distance between the bottom of the alumina plate and the probe tip is 4 cm. Tungsten wire was used for the probe material, with an exposed tip length of 5mm and tip diameter of 127µm. The Langmuir probe employs a self-compensated design[17,18], with a large area auxiliary electrode and a 200pF capacitor. A self-resonating 100 µH inductor—set to the 13.56 MHz frequency used for the RF power source—is inserted in series with the probe to eliminate RF disturbances to the probe signal and development of RF across the probe. A Fourier transform on the current through the probe, with the plasma on, suggests that this design reduces the radio frequency harmonics below the detection limit of our current setup.

The sweeping voltage (B in Figure 4.1(b)) required for Langmuir probe measurements is provided by a Wavetek 182 signal generator pushing a triangular wave at 10Hz which is amplified using a Kepco BOP 100-1M. The probe current is monitored by measuring the potential drop across a 30Ω resistor. A Teledyne DA1855A differential amplifier is used to measure this voltage drop. The signals are recorded with a PicoScope 5442A digital oscilloscope performing a weighted average over 667 waveforms with an

ultimate time-to-measure of three minutes per I-V curve. The Langmuir probe measurement routine is the following:

1. The whole system is evacuated at a base pressure of 10^{-6} Torr

2. The Ar-H_2 gas mix is flowed into the system and a plasma discharge is ignited in the primary reactor.

3. The I-V characteristic of the Langmuir probe is acquired in dust-free conditions

4. The whole system is evacuated at a base pressure of 10^{-6} Torr

5. The Ar-H_2-C_2H_2 gas admixture is flowed into the system. The discharge is ignited in both the secondary reactor, hence starting the production of graphitic particles, and in the primary reactor. I-V characteristics are measured under dusty conditions while varying the desired parameter, such as input power.

6. The system is again evacuated down to a base pressure of 10^{-6} Torr. Point 2 and point 3 are repeated.

7. The EEDFs derived from 3 and 6 are compared to ensure that effects arising from the accumulation of graphitic nanoparticles at the probe tip are negligible.

As a precautionary measure, the probe tip is restored to pristine condition by applying a sufficiently positive bias for 10 seconds to lead to visible glowing of the probe tip. The process, induced by joule heating at the probe tip, effectively removes any deposit from the probe surface.

The current and voltage waveforms are smoothed via Savitzky-Golay averaging. Following the Druyvesteyn method[19], both the electron energy distribution function

(EEDF), $F(E)$, and the electron energy probability function (EEPF), $f(E)$, are determined from the measured I-V from the equation described in (1) and (2):

$$F(E) = \frac{\sqrt{8m_e}}{e^3 A_p} \sqrt{E} \frac{dI_e^2}{d^2 |V_p - V|} \qquad (1)$$

$$f(E) = \frac{F(E)}{\sqrt{E}} \qquad (2)$$

Where E is the energy, m_e the mass of an electron, e the charge of an electron, A_p the area of the probe surface, I_e the electron current, V_p the plasma potential, and V the sweeping voltage applied to the probe tip. The plasma potential V_p corresponds to the inflection point in the I-V characteristic. Additional adjacent averaging is performed on the second derivative to obtain $F(E)$. The electron - n_e - and ion - n_{ion} - densities, electron temperature - T_e - and the particle charge - Q - were calculated from $F(E)$ using the equations (3-6):

$$n_e = \int_0^\infty F(E) dE \qquad (3)$$

$$n_{ion} = \frac{I_{ion}}{2eR_p L_p \sqrt{\frac{2e|V_p - V|}{m_{ion}}}} \qquad (4)$$

$$T_e = \frac{2}{3} n_e^{-1} \int_0^\infty E \, F(E) dE \qquad (5)$$

$$Q = \frac{n_{ion} - n_e}{n_{particle}} \qquad (6)$$

Where R_p and L_p are the probe tip radius and length respectively, m_{ion} is the mass of an ion and $n_{particle}$ is the particle density in the plasma.

4.3 Results and Discussion

In the nanoparticle generation cell, the production parameters were optimized to give graphitic particles. This structure, due to its higher electrical conductivity as compared to, for instance, amorphous carbon, minimizes the perturbation in the Langmuir probe measurement resulting from dust accumulation at the probe tip. More details about the process employed for the fabrication of the carbon nanoparticles and the mechanism leading to their graphitization in the plasma environment are reported in our previous publication[20]. The carbonaceous nanomaterials produced in the secondary reactor were collected and characterized via TEM and Raman Spectroscopy. The results are detailed in Figure 4.2. Nanoparticles with a collapsed-graphene morphology (see Figure 4.2(a)) and a fairly monodisperse particle size distribution (see Figure 4.2 (b)), with an average diameter 14 nm and standard deviation 1.7 nm, are observed from the TEM scans.
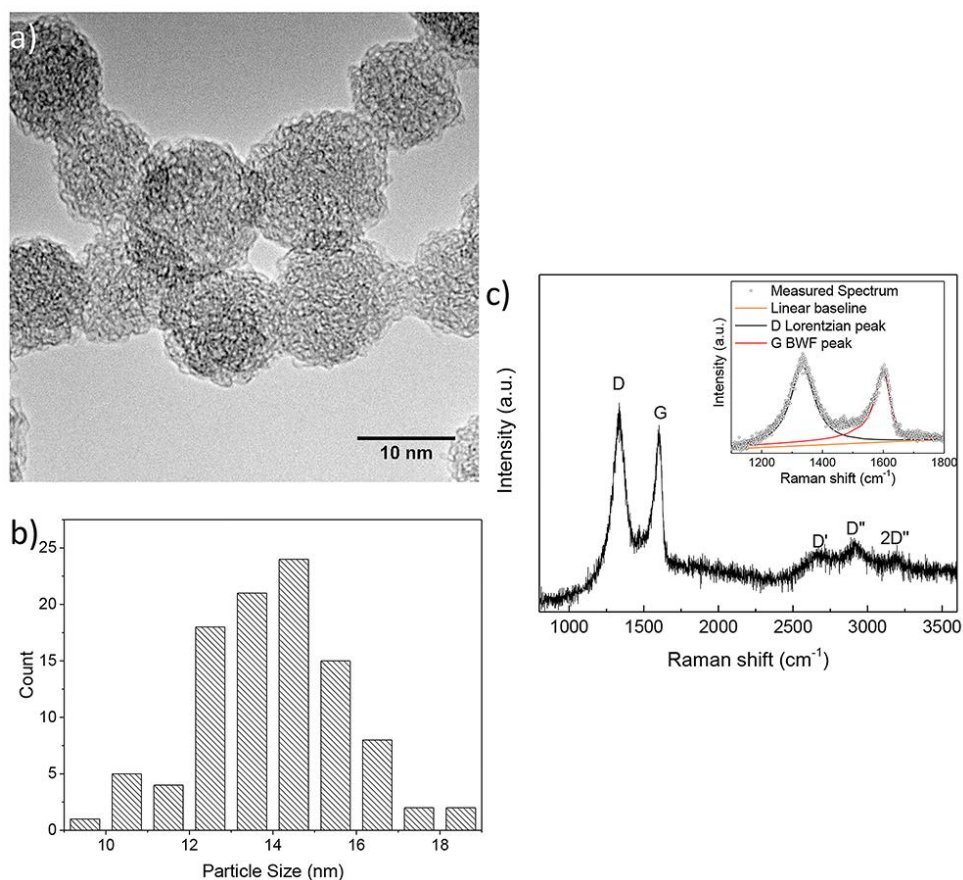
Figure 4.2. (a) high magnification TEM scan and (b) particle size distribution of the carbon nanomaterials produced by the nanoparticle generation cell. (c) Corresponding Raman spectrum of the synthesized materials (the deconvolution routine employed for the calculation of the I_D/I_G and m/I_G ratios is depicted in the inset).

The corresponding Raman spectrum (see Figure 4.2(c)) shows two sharps peaks around 1330 cm^{-1} and 1610 cm^{-1}, the D and G modes respectively, and three smaller but still well-visible features around 2650 cm^{-1}, 2900 cm^{-1} and 3200 cm^{-1}, the second order D', D'' and 2D' modes.

These results suggest a high content of graphitic carbon in produced nanomaterials. The measured signal was deconvoluted with a fitting routing comprising a Lorentzian peak for the D component, a BWF peak for the G component and a linear baseline with slope

60

m. The resulting values of I_D/I_G intensity ratio, around 1.15, and m/I_G, around 1.9 µm, are the typical signature of a highly graphitic material characterized by a low hydrogen content, further corroborating the previously described TEM analysis. The graphitic nanoparticles, produced in the particle generation cell, were dosed in the primary plasma during the Langmuir probe scans in dust-rich conditions. While, as described in the experimental section, the probe tip was cleaned after every measurement to prevent an excessive accumulation of nanoparticles at the probes surface, the particle accumulation at the tip during the I-V scans could still impair the reliability of measurements. To verify that the perturbations arising from the growth of a nanoparticle coating on the probe tip could, as a first approximation, be considered negligible we performed three experiments. We measured $f(E)$ in a dust-free Ar-H$_2$ with fixed RF input power before particle injection, directly after 12 minutes of carbon particle injection, and after cleaning the probe surface via electron bombardment. The results are illustrated in Figure 4.3(a). No major changes were observed in terms of $f(E)$, T_e, n_e, or n_{ion} for the three conditions. The properties of the dust-free Ar-H$_2$ plasma as a function of applied RF input power were then investigated in the dust-free regime. The results for $f(E)$ are depicted in Figure 4.3(b), and Figure 4.3(c) shows n_{ion}, n_e and T_e as a function of RF input power. n_{ion} was calculated from equation (3) reported in the experimental session. Its value depends on the ion atomic mass m_{ion}. This introduces difficulties, since the dominant ion in an Ar-H$_2$ mixture is not known a priori, and the precise determination of the ion density is necessary to reliably obtain the nanoparticle charge using equation (5). Two primary ions are identified in the related literature as the most likely dominating species: Ar^+ and H_3^+ [21-23]. For the composition

61

utilized in this investigation (with a 2% H_2 volume fraction) and based on both experimental and theoretical studies on non-thermal plasmas generated in this mixture, Ar^+ is expected to be the dominant ion. Nevertheless, H_3^+ may contribute significantly to the probe current in the ion saturation regime because of its lower atomic mass and higher electrical mobility.
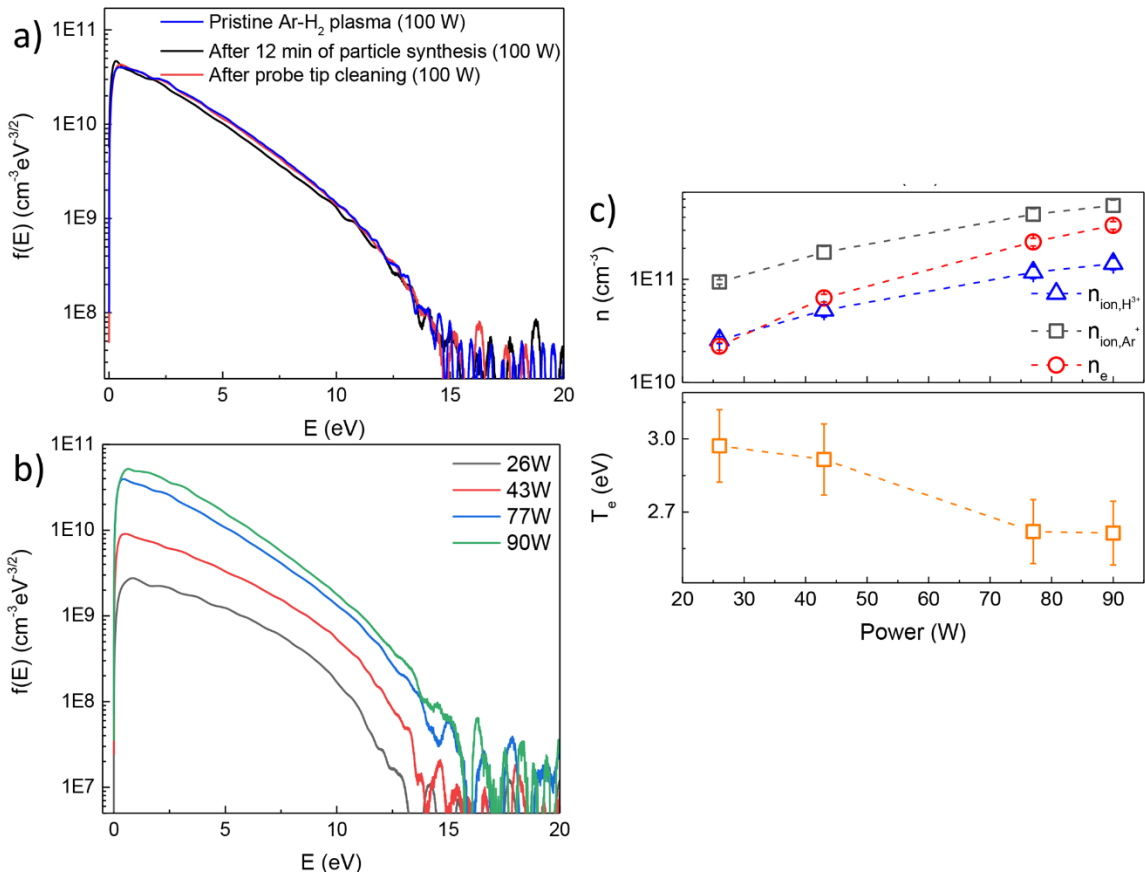
Figure 4.3. a) f(E) measurements taken for a dust free Ar-H_2 before particle injection, directly after 12 minutes of particle injection, and after cleaning the probe surface via electron bombardment. Notably, the nanoparticle generation cell was operated for a time significantly longer (12 min) than the one required for a single Langmuir probe measurement (3 min). b) f(E), c) n_{ion}, n_e and T_e measured in a pristine Ar-H_2 plasma for increasing plasma powers.

In order to establish which ion mass is more appropriate to use for the determination of the ion density, we have first performed measurement in a pure argon plasma (results not shown here for brevity), confirming that the ion and electron densities obtained using equations (2) and (3) are close (within 20%) of each other. We have then performed measurements in the Ar-H$_2$ system as a function or the RF power. In figure 4.3(c) we report the electron density calculated using equation (2) and the ion densities calculated using equation (3) assuming an ion atomic mass corresponding to Ar$^+$ and H$_3$$^+$ respectively. At low RF power, for a plasma density lower than 5×10^{10} cm^{-3}, the electron density is close to the ion density value obtained using the ion mass of H$_3$$^+$. At higher power the electron density value approaches the ion density calculated using the Ar$^+$ mass. In agreement with the related theory, as the plasma power is increased, the electron temperature, also shown in figure 4.3(c), decreases[24]. We point out that the nanoparticle heating models discussed in the literature, when dealing with particles immersed in an argon-hydrogen plasma, often assumes that the dominant ion is argon, i.e. the energy released to the particle by a charge recombination event corresponds to the ionization potential of argon[25,26]. Our experimental observation suggest that it would be more appropriate to assume that the heat flux is due to H$_3$$^+$ recombination. The properties of the Ar-H$_2$ plasma as a function of the RF power were investigated upon injection of the graphitic nanoparticles from the particle generation cell. Figure 4.4(a) and Figure 4.4(b) report the measured $f(E)$, n_{ion}, n_e and T_e as a function of the power coupled in the primary plasma. H$_3$$^+$ is assumed to be the dominant ion in the dust-rich plasma, since both the electron and ion density are low (well below 5×10^{10} cm^{-3}). The dust density in the plasma is calculated from the material mass

production of the particle generation cell, 1.6 mg/hr, and is highly dependent on the assumed material density. If we assume that the particles have a density corresponding to that of bulk graphite, 2.267 g/cm^3 [27] the nanoparticle density is 7.34×10^7 cm^{-3}. On the other hand, although Raman suggest their graphitized structure, TEM indicates that their morphology resembles that of crumpled graphene, whose density is likely much lower than that of graphite. Due to a lack of precise density values for this case, we assume the density of amorphous carbon, 1.4 g/cm^3 [27], and find that the corresponding nanoparticle density is 1.19×10^8 cm^{-3}. We expect the nanoparticles density to fall between these two limiting cases.
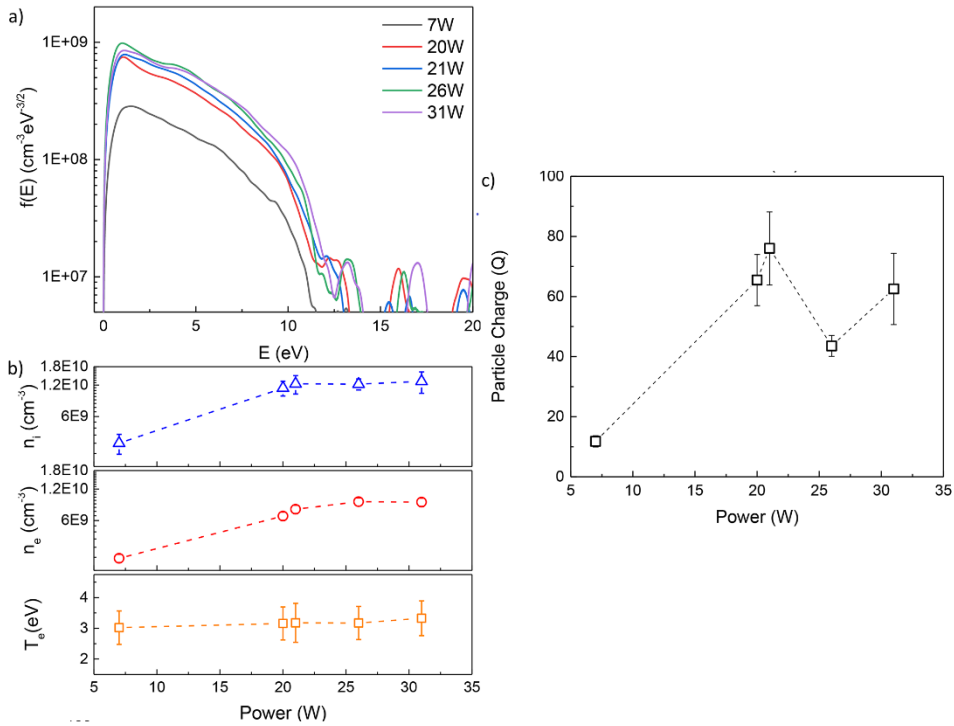
Figure 4.4. (a) *f(E)* collected across a range of increasing plasma power in a dust rich Ar-H$_2$ plasma. (b) Corresponding n_{ion}, n_e and T_e for increasing plasma power. c) Variation of number of charges per particle as a function of the plasma power.

From figure 4.4(b), the trend in ion density points to the presence of nanoparticles having a deep effect on the power coupling to the discharge. The energy distributions shown in figure 4.4(a) are similar to those shown in figure 4.3(b) for the low power limiting case. Although the electrical power is supplied to the reactor via a three-turn planar coil, the plasma in the pristine case is likely operating in a capacitively coupled mode at such low input powers. The low plasma density and relatively high electron temperature in the low power regime (see figure 4.3(c)) are consistent with this observation. We therefore conclude that the discharge is operating in capacitive mode for the dusty plasma case as well. We have found that any attempt at further increasing the input power for the dusty plasma case only leads to the onset of instabilities which are easily distinguishable by naked eye (rapid flickering of the plasma emission). We have found that the Langmuir probe measurement is impossible to perform while these instabilities are present because of wide fluctuations in current. The instabilities are clearly induced by the presence of dust, as observed by several other research groups[28-30], since it is trivial to operate the pristine plasma at significantly higher input power levels, as demonstrated by the energy distributions and by the plasma densities reported in figure 4.3. For the dusty plasma case, an increase in nanoparticle density, which can be achieved by increasing the acetylene flow rate to the secondary nanoparticle-producing plasma, only exacerbates this problem, i.e. facilitates the onset of instabilities.

The electron temperature in the dusty plasma case (figure 4.4(b)) is slightly higher than in the pristine case (in the low plasma input power regime, as seen in figure 4.3(c)). The presence of dust is expected to lead to an increase in electron temperature compared

to the pristine case because of additional loss of ion-electron pairs to the particles surface. While this relatively low electron temperature in the dusty plasma case may seem surprising, we should stress that the nanoparticle density is relatively low—an order of magnitude lower than the electron density. As stated earlier, any attempt at increasing the nanoparticle density only resulted in the onset of instabilities that make the operational window of the discharge particularly narrow.

The presence of dust is confirmed by the fact that the ion density exceeds the electron density, as shown in figure 4.4(b). In figure 4.4(c) we plot the number of elementary charges per particle as a function of electrical power input. The number of charges per particle does not monotonically increase with power, instead reaching a maximum around 20 W to then decrease at higher input power.

To better clarify the origin of this behavior, we have compared the measured plasma properties with a self-consistent steady-state zero-dimensional model for low-pressure argon plasmas containing nanoparticles which is solved numerically. At this time, hydrogen has not been included in the model for simplicity. An additional simplification has been done in assuming that the electron energy distribution is Maxwellian. The model comprises four equations (7)–(10) which are well accepted as appropriate descriptors of particle charging in plasmas[31]. Equation (7) is based on the orbital-motion-limited theory and describes the collision frequency between charged species and particles $v_{e,ion}$:

$$
v_{e,ion} = \begin{cases} n_{e,ion} S \sqrt{\dfrac{k_B T_{e,ion}}{2\pi m_{e,ion}}} \exp\left(-\dfrac{q_{e,ion}\Phi}{k_B T_{e,ion}}\right), & q_{e,ion}\Phi \geq 0 \\[4mm] n_{e,ion} S \sqrt{\dfrac{k_B T_{e,ion}}{2\pi m_{e,ion}}} \left(1 - \dfrac{q_{e,ion}\Phi}{k_B T_{e,ion}}\right), & q_{e,ion}\Phi \leq 0 \end{cases} \tag{7}
$$

Where r_p is the particle radius, $S = 4\pi r_p{}^2$ is the particle surface area, $\Phi = \frac{Z_k}{4\pi\varepsilon_0 r_p}$ is the

particle potential, $Z_k = k{\cdot}e$ is the particle charge (e being the electron elementary charge

and k is number of elementary charges carried), $n_{e,ion}$ is the electron (ion) density, $m_{e,ion}$ is

the electron (ion) mass, k_B is the Boltzmann constant, $T_{e,ion}$ the electron (ion) temperature,

and $q_{e,ion}$ is the respective electron (ion) charge. Equation (8) describes the quasi-neutrality

of the discharge:

$$n_e + kn_{particle} = n_{ion} \qquad (8)$$

Equation (9) describes the ionization balance and takes into account ion production by

electron-induced ionization and ion loss to the walls and to the particles.

$$n_e v_{ionization} V = n_{ion} \left(\frac{D_a}{l}\right) A + n_p v_{ion} V \qquad (9)$$

Where l is the characteristic diffusion length, D_a is the ambipolar diffusion length,

$v_{ionization}$ stands for total ionization frequency, V is the plasma volume, and A is the

surface area bounding the plasma volume. $v_{ionization}$ results from the direct integration of

the Ar ionization cross-section over the electron energy distribution:

$$v_{ionization} = < N\sigma_{ion} U_{th} >$$

Where N is the argon gas density at 300K and at a pressure of 150 mTorr, U_{th} is electron

thermal velocity and σ_{ion} is the ionization cross-sections. Equation (10) describes the

power balance in the plasma discharge and takes into account the power provided by radio-

frequency field as well as power loss to excitation and ionization events in the discharge

volume, power loss due to ion acceleration through the sheath, through electron-neutral

momentum transfer, and to the nanoparticles through the collection of electrons.

$$P_{rf} = n_e v_{ex} E_{ex} V + n_e v_{ionization} E_{ion} V + n_{ion} \left(\frac{D_a}{l}\right) A \left(\frac{V_{sh}}{2}\right) + \left(\frac{2m_e}{m_{ion}}\right) \frac{3}{2} k_B (T_e -$$

$$T_g) n_e v_m V + n_p V \int_{-\Phi}^{\infty} E\, e\, dv_e\, (\Phi, f_0, E) \qquad (10)$$

Where P_{rf} is the radio-frequency power, $v_{ex} = <N\sigma_{ex}U_{th}>$ is the total excitation frequency, $v_m = <N\sigma_m U_{th}>$ is the total momentum transfer frequency, E_{ex} is the effective electronic excitation energy, E_{ion} is the ionization energy, and T_g is the Argon gas temperature (300K). The collision cross sections are taken from the JILA database[32]. We also account for thermionic emission by including an emission frequency into the nanoparticle charge balance. The thermionic emission frequency which is described by Richardson's law in equation(11):

$$v_{th} = S \left(\frac{1}{e}\right) A_0 T_p^2 \exp\left(-\frac{W}{k_B T_p}\right) \qquad (11)$$

Where v_{th} stands for thermionic emission frequency, T_P is the particle temperature, $A_0 = \frac{4\pi m_e k_B^2 e}{h^3}$ is the Richardson constant, h stands for Planck's constant, and W is the work function.
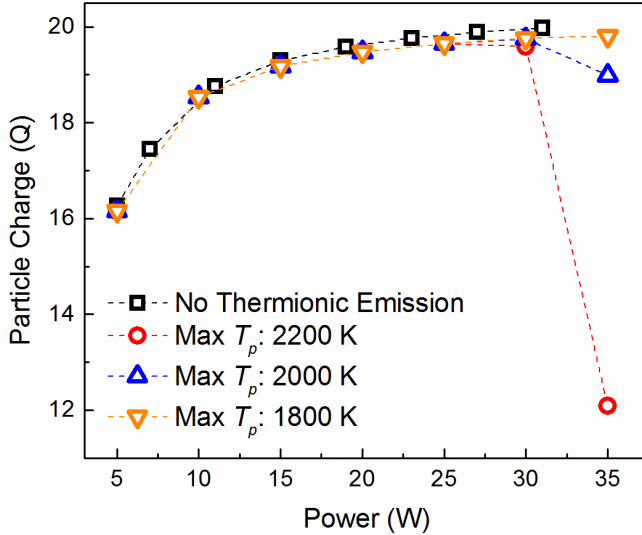
Figure 4.5. Variation of the number of negative charges per particle as a function of the plasma power obtained from the self-consistent model by employing the density of graphitic carbon. Thermionic emission is included in the model, T_p is the assumed maximum nanoparticle temperature.

The particle temperature is assumed to vary linearly with input power, from 300 K at 5 W to maximum temperatures of 1800, 2000 and 2200 K at 35 W. The results from this self-consistent model are shown in figure 4.5. The nanoparticle size and density, based on the experimental values, are 14 nm and 1.6×108 cm^{-3}. In figure 4.5, we plot the number of elementary charges carried by the particles as a function of input power, which increases slightly from 16 to 20. Considering the thermionic emission effect, a stark drop in particle charge at high particle temperatures is observed.

4.4 Conclusions

We have developed a test-bed for the characterization of nonthermal plasmas which are controllably dosed with nanoparticles independently produced in a secondary reactor. This approach allows for investigating the properties of a dusty plasma which is completely decoupled from the kinetics of nucleation and growth. As an example, we have applied this approach to the case of an Ar–H_2 non-thermal plasma dosed with graphitic carbon nanoparticles and investigated how input RF power affects parameters such as ion and electron density, electron temperature, and average particle charge. We have used a Langmuir probe for plasma characterization and found that this two-plasma reactor approach leads to a situation that is quite forgiving with respect of probe surface contamination. We have also found that while this approach allows accessing, in principle, a broad experimental parameters space, the onset of dust-triggered plasma instabilities limits the actual range of parameters in which the characterization can be successfully performed. Nevertheless, the results from this first study suggest that the power coupling to the discharge is severely affected by the presence of dust. As RF power is increased, the charge carrier density does not continuously increase, and the average nanoparticle charge decreases even at moderate input power. This behavior cannot be captured by a particle charging model which is based on a simple, yet broadly utilized, set of governing equations. Additional assumptions on possible mechanisms that can lead to loss of negative charges, such as thermionic emission, are needed to qualitatively capture the experimental observations. These results suggest that the details of plasma-nanoparticle interaction are far from fully understood.

4.5: References

(1)   Selwyn G.S., Singh J., and Bennett R.S. *Journal of Vacuum Science & Technology A*. **7**, 2758-2765 (1989).

(2)   Selwyn G.S., Heidenreich J.E., and Haller K.L. *Journal of Vacuum Science & Technology A*. **9**, 2817-2824 (1991).

(3)   Kortshagen U.R., Sankaran R.M., Pereira R.N., Girshick S.L., Wu J.J., and Aydil E.S. *Chemical Reviews*. **116**, 11061-11127 (2016).

(4)   Mariotti D. and Sankaran R.M. *Journal of Physics D-Applied Physics*. **43** 323001 (2010).

(5)   Alvarez Barragan A., Ilawe N.V., Zhong L., Wong B.M., and Mangolini L. *The Journal of Physical Chemistry C*. **121**, 2316-2322.

(6)   Zhang H., Zhang R., Schramke K.S., Bedford N.M., Hunter K., Kortshagen U.R., and Nordlander P. *ACS Photonics*. **4**, 963-970 (2017).

(7)   Kessler V., Gautam D., Hulser T., Spree M., Theissmann R., Winterer M., Wiggers H., Schierning G., and Schmechel R. *Advanced Engineering Materials*. **15**, 379-385 (2013).

(8)   Nava G., Fumagalli F., Gambino S., Farella I., Dell'Erba G., Beretta D., Divitini G., Ducati C., Caironi M., Cola A., and Di Fonzo F. *Journal of Materials Chemistry C*. **5**, 3725-3735 (2017).

(9)   Holman Z.C., Liu C.-Y., and Kortshagen U.R. *Nano Letters*. **10**, 2661-2666 (2010).

(10)   Thimsen E., Johnson M., Zhang X., Wagner A.J., Mkhoyan K.A., Kortshagen U.R., and Aydil E.S. *Nat Commun*. **5** (2014).

(11)   Barragan A.A., Nava G., Wagner N.J., and Mangolini L. *Journal of Vacuum Science & Technology B, Nanotechnology and Microelectronics: Materials, Processing, Measurement, and Phenomena*. **36**, 011402 (2018).

(12)   Greco E., Nava G., Fathi R., Fumagalli F., Del Rio-Castillo A.E., Ansaldo A., Monaco S., Bonaccorso F., Pellegrini V., and Di Fonzo F. *Journal of Materials Chemistry A*. **5**, 19306-19315 (2017).

(13)   Zhong L., Guo J., and Mangolini L. *Journal of Power Sources*. **273**, 638-644 (2015).

(14)   Godyak V.A., Piejak R.B., and Alexandrovich B.M. *Plasma Sources Science and Technology*. **1**, 36 (1992).

(15)   Godyak V.A., Piejak R.B., and Alexandrovich B.M. *Journal of Applied Physics*. **73**, 3657-3663 (1993).

(16)   Bilik N., Anthony R., Merritt B.A., Aydil E.S., and Kortshagen U.R. *Journal of Physics D: Applied Physics*. **48**, 105204 (2015).

(17)   Sudit I.D. and Chen F.F. *Plasma Sources Science and Technology*. **3**, 162 (1994).

(18)   Chatterton P.A., Rees J.A., Wu W.L., and Al-Assadi K. *Vacuum*. **42**, 489-493 (1991).

(19)   Druyvesteyn M.J. *Zeitschrift für Physik*. **64**, 781-798 (1930).

(20)   Woodard A., Shojaei K., Nava G., and Mangolini L. *Plasma Chemistry and Plasma Processing*. (2018).

(21)   Mason R.S., Miller P.D., and Mortimer I.P. *Physical Review E*. **55**, 7462-7472 (1997).

(22)   Bogaerts A. and Gijbels R. *Journal of Analytical Atomic Spectrometry*. **15**, 441-449 (2000).

(23)   Laidani N., Bartali R., Tosi P., and Anderle M. *Journal of Physics D: Applied Physics*. **37**, 2593 (2004).

(24)   Lee H.-C., Seo B.H., Kwon D.-C., Kim J.H., Seong D.J., Oh S.J., Chung C.-W., You K.H., and Shin C. *Applied Physics Letters*. **110**, 014106 (2017).

(25)   Mangolini L. and Kortshagen U. *Physical Review E*. **79**, 026405 (2009).

(26)   Kramer N.J., Anthony R.J., Mamunuru M., Aydil E.S., and Kortshagen U.R. *Journal of Physics D: Applied Physics*. **47**, 075202 (2014).

(27)   Robertson J. *Advances in Physics*. **35**, 317-374 (1986).

(28)   Mikikian M, Couëdel L, Cavarroc M, Tessier Y and Boufendi L *J. Phys*. **9,** 268 (2007).

(29)   Pacha K A, Heinrich J R, Kim S H and Merlino R L *Phys. Plasmas* **19,** 014501 (2012).

(30)   Heinrich J R, Kim S H and Merlino R L *Phys. Rev. E* **84**, 026403 (2011).

(31)   Kortshagen U and Bhandarkar U 1999 *Phys. Rev. E* **60,** 887–98 (1999).

(32)   Yamabe C, Buckman S J and Phelps A V *Phys. Rev. A* **27,** 1345.

Chapter 5: Electron emission from particles strongly affects the electron energy distribution in dusty plasmas

5.1 Introduction

Low-pressure, low-temperature non-thermal dusty plasmas are weakly ionized gases containing particulate of condensed matter. They are ubiquitous in industrial and academic plasma laboratories. The formation of dust in industrial processing plasmas was initially treated as a source of contamination.[1, 2] That view has progressively evolved to one in which plasmas are a viable and controllable route for nanopowder fabrication. Despite the many promising reports confirming the potential of plasma-produced nanoparticles,[3-10] an increased understanding of the fundamental physics of dusty plasmas is in our opinion necessary to further advance this field. In particular, the mutual interaction between plasma and the nanoparticles dispersed within it is far from being fully understood, a problem exacerbated by the fact that this is a notoriously difficult system to probe experimentally. While it is accepted that the recombination of plasma-produced species at the surface of the nanoparticles can induce heating and crystallization of even high melting point materials,[7, 11-13] its complementary aspect, i.e. how the presence of particles affects the plasma, has received significantly less attention. The current understanding is that particles suspended in a plasma effectively behave as electron-sinks, draining electrons from the discharge and hence becoming unipolarly negatively charged. This effect induces a reduction of the plasma electron density and, correspondingly, an increase in the electron temperature to support the discharge ionization balance. Their large

attachment cross section depletes the electron energy distributions at potentials higher than the nanoparticle floating potential.

We show that, at low pressures, the presence of nanoparticles has more profound effects than previously expected. Using a Langmuir probe, we have found that a large fraction of the electron population has energies 2-3 eV above the plasma potential. The current working hypothesis is that the nanoparticles behave as distributed electron emitters—electrons are ejected from the nanoparticles via electron emission and injected into the plasma with an energy corresponding to the nanoparticle floating potential. This hypothesis is strengthened by a collaborator and fellow Ph.D. student, Kamran Shojaei, through his efforts in solving the nanoparticle charge balance by accounting for several mechanisms—photoelectric emission, secondary emission due to impact of charged species at the particles' surface, thermionic emission and electron evaporation due to the negative charge already present on the particle. Incorporating this into a theoretical solution of the electron energy distribution function leads to the same phenomenon reported here: electrons are ejected from the particle surface via electron emission and injected into the plasma with an energy corresponding to the nanoparticle floating potential. Overall, this is the first report of the direct measurement of the nanoparticle floating potential, and correspondingly charge, in a non-thermal plasma.

5.2 Experimental Setup

5.2.1: Langmuir measurement system and carbon nanoparticle production

A schematic of the experimental setup is reported in Figure 5.1. The experiments were performed in a vacuum chamber equipped with an inductive planar coil RF source for plasma generation and a Langmuir probe for the measurement of the discharge properties.[14] This primary chamber is dosed with carbon nanoparticles produced from the dissociation of acetylene (C_2H_2) in an auxiliary plasma, the particle production cell. More details about the working principle of the system are detailed in our previous publications.[15] The RF power in the production cell is maintained at 100 W, while the power in the primary chamber ranged from 60 W to 120 W. Full consumption of C_2H_2 in the particle production cell was verified with a residual gas analyzer measurement. The nanoparticle injection-rate in the primary chamber was carefully measured with a gravimetric method. A stainless-steel mesh was attached at the exit of the injection tube to capture the carbonaceous particles produced by the production cell. The injection rate was calculated from the total collected mass (measured with a Sartorius ENTRIS64-1S microbalance).
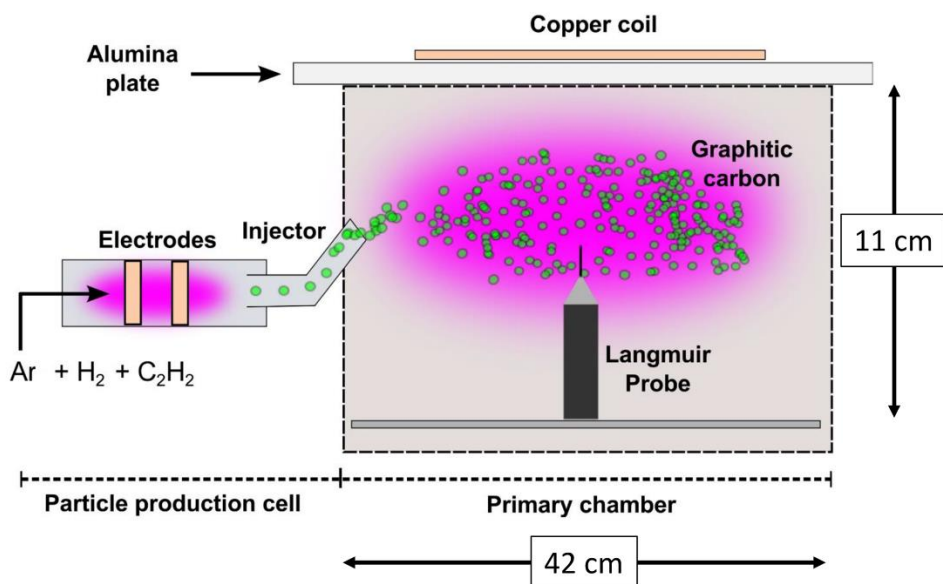
Figure 5.1. Schematic of the two-stage system used in the experiments. The gas flown was a mixture of 30 sccm Ar, 1.5 sccm H_2, and 3 sccm C_2H_2, with a pressure differential of 1.5 Torr:15 mTorr in the particle production cell and primary chamber maintained by a 2 mm orifice. In both reactors, independently controlled radio frequency (13.56Mhz) generators are connected to L-type matching networks to maintain the discharge.

5.2.2: Optical measurement of particle density

In order to estimate the particle density in the primary chamber, laser scattering intensity measurements were performed in the system (see Figure 5.2).
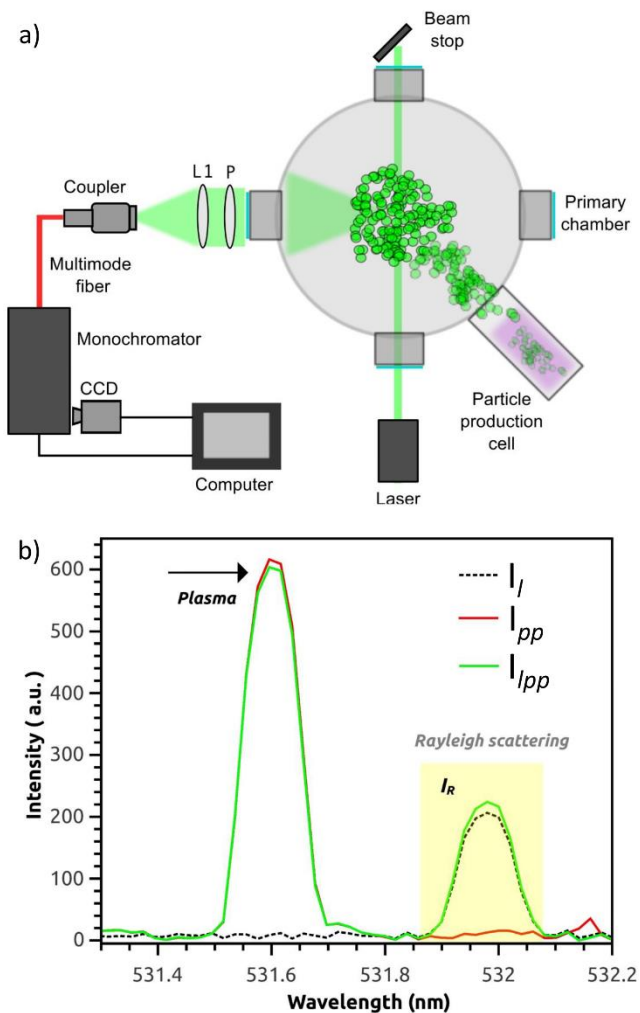
Figure 5.2. Schematic of the setup employed for the measurement of the Rayleigh scattering from the carbon particles suspended in the primary plasma (a). A 532 laser (500 mW power) enters the primary chamber through a highly transmitting viewport. The Rayleigh scattering is collected from a second viewport (b) in a 90-degree configuration.

A continuous wave (C.W) laser of $\lambda = 532$ nm, spot size of 500 μm and laser power of P = 1.5 W, was introduced in one of the window ports of the primary chamber. The Rayleigh scattered light from graphitic carbon nanoparticles was collected in a 90-degree configuration from a second port of the primary chamber. A linear polarizer was located right after the collection window to reduce the laser light noise produced by the scattered

reflections of the stainless-steel chamber's interior. The scattered light from the graphitic particles was focused into a multimode glass fiber with an air-spaced doublet collimator (Thorlabs), connected to a triple grating imaging spectrometer (Acton Spectra Pro, Princeton Instruments). The inlet grating from the monochromator was closed to 30 µm width to obtain high-resolution spectra and differentiate scattered laser light from the Ar-H_2 plasma emission spectrum. The emission spectra were captured by the CCD camera (1024×256) located at the exit monochromator's slit, with an acquisition time of 250 ms and a total recording of 300 frames. The spectrometer was connected to a computer to visualize and record the emission spectrum. The Rayleigh scattering measurements were performed under an internal total pressure of 20 mTorr, a mass flow rate of 30 sccm Ar, 1.5 H_2 and 3 sccm of C_2H_2 with radio frequency (RF) power sweep from 20 to 120 W, in steps of 20 W. The scattered signal intensity from the graphitic particles I_P, trapped in the main chamber, was calculated as:

$$I_p = I_{lpp} - (I_l + I_{pp}) \qquad (1)$$

Where I_l is the background intensity of the laser collected in absence of particles and trapping plasma (i.e. only argon and hydrogen gases were flowing in the chamber); I_{lpp} is the scattered light intensity in the presence of laser, particles and the Ar − H_2 trapping plasma; and I_{pp} is the intensity of the plasma emission with particles flowing in the absence of the laser. Equation 1 was hence used to obtain a quantitative measurement of the Rayleigh intensity peak of the particles, I_P, subtracting the plasma emission and laser

background contributions. The emission spectrum of I_l, I_{lpp} and I_{pp} are shown in Figure 5.2b.

Theoretically, the Rayleigh scattering intensity is defined as $I_P = I_o \cdot n_p \cdot \sigma_p$, where I_o is the incident intensity of the laser, n_p is the particle density and σ_p is the scattering cross section of carbon particles.[16]

$$\sigma_p = \frac{2\pi^5}{3} \left| \frac{m^2 - 1}{m^2 + 1} \right|^2 \frac{(2R)^6}{\lambda^4} \qquad (2)$$

R, the radius of the particles, λ, the wavelength of the scattered light, and m, the complex refractive index of carbon m = n+ ik, with $n = 1.915$ and $k = 0.952$, where n represents the refractive index and k represents the extinction coefficient of the material. We carried out measurements of the scattered light intensity for argon at a pressure of 1 atmosphere to calibrate the response of our detection system, i.e. to perform a relative measurement of the scattering intensity with respect of a known scattering medium. The resulting scattering intensity is $I_G = I_o \cdot n_{Ar} \cdot \sigma_{Ar}$, with $n_{Ar} = 2.69 \times 10^{19}$ cm^{-3} being the argon number density, as calculated using ideal gas law, and $\sigma_{Ar} = 4.45 \times 10^{-27}$ cm^2 being the scattering cross section from argon.[17] The particle density n_p can then be calculated as:

$$n_p = \frac{I_P}{I_G} \frac{n_{Ar} \sigma_{Ar}}{\sigma_P} \qquad (3)$$

It is important to mention that, in the described analysis of the light scattering signal, we assumed the particles to be isolated and non-interacting spheres. We expect this to be a valid assumption for the case of nanoparticles which are electrostatically stabilized in the plasma.

5.3 Results and Discussion

The primary plasma of the setup was dosed with graphitic carbon nanoparticles produced in an auxiliary RF discharge placed at the inlet of the primary chamber. This particle generation cell fully consumes acetylene and converts it into the graphitic particles shown in the inset of Figure 5.3a.[15, 18] This two-stage reactor allows investigating the influence of nanoparticles on the plasma properties by decoupling it from the nucleation and growth phase, which occurs in a spatially separated particle generation cell. As already described in Chapter 4, the use of conductive particles, such as the graphitic ones used here, prevents the formation of an insulating layer on the probe tip and enables its functionality in dust-rich discharges.[19, 20] An in-depth description of the set-up, its working principle, the method and theory for obtaining the Langmuir probe measurements inside the dusty environment are detailed in our previous work.[15]
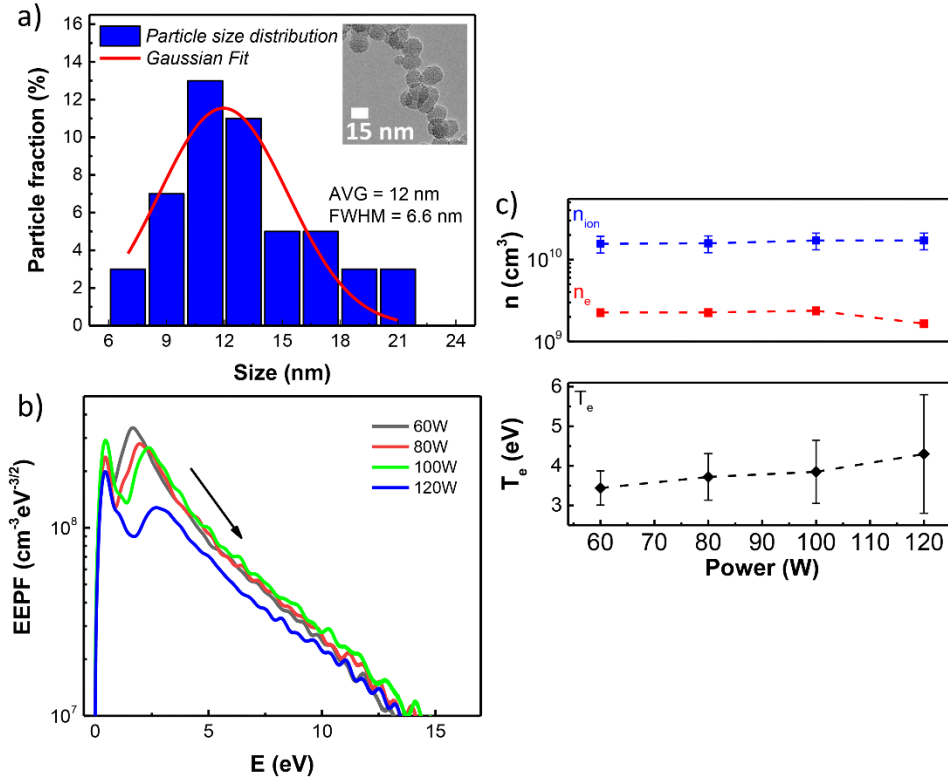
Figure 5.3. Particle size distribution measured from TEM analysis and fitted with a gaussian profile (a). The inset show a TEM micrograph of the synthesized particles. Measured EEPF (b), n_e, n_{ion} and T_e as a function of the input plasma power (c).

The particle size distribution for the graphitic carbon nanoparticles is shown in Figure 5.3a. The average particle size is 12 nm with a standard deviation of 3.8 nm. Figure 5.3b shows the electron energy probability distribution functions (EEPFs), $f(\varepsilon)$, measured in the primary chamber at varying input powers, with carbon nanoparticles injected in the plasma. The electron energy distribution functions (EEDFs), $F(\varepsilon)$, were derived from the probe characteristics using the Druyvestein method.[21] The EEPF $f(\varepsilon)$ is defined as $F(\varepsilon) \cdot \varepsilon^{-1/2}$. The EEPFs shows a broad peak in the 2-4 eV range with peak position varying smoothly and increasing with increasing input power. Peaks in the EEPF have been reported in afterglow discharges, in the high-energy tail of the distribution because of latent Penning

ionization.[22] However, in that scenario the peak in the electron energy does not vary with process parameters since it is constrained by the metastable energy and ionization potential of the utilized gasses. Our observation is clearly different. We measure a shift as a function of RF power, with exactly the same gas composition. Moreover, we have never observed the peak under pristine conditions, i.e. without particles, as can be seen in Figure 5.4. This strongly suggests that the peak in the EEPFs is correlated to the presence of particles in the plasma.
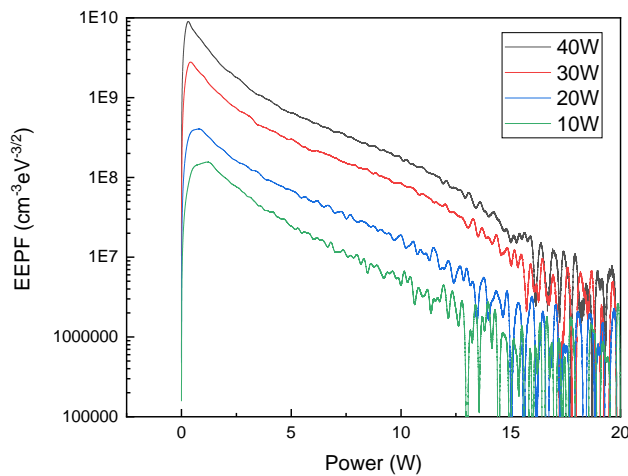
Figure 5.4. Measured EEPF under pristine, Ar-H$_2$ only conditions; no secondary peak emerges as observed with particles.

It is also interesting to point out that potential range in which the peak is observed, 2-3 volts below the plasma potential, is strikingly close to the expected nanoparticle floating potential for this kind of low-pressure discharges, as predicted by the orbital motion limited theory. Electrons ejected from a negatively charged particle will gain an energy equal to the floating potential as they cross the sheath and enter the plasma. To

validate this hypothesis, we first proceed to measure the nanoparticle charge in the plasma volume by measuring the deficit between ion and electron densities. Under the assumption of quasi-neutrality, the average charge per particle Q can be calculated using the following equation.

$$n_e = n_{ion} - Qn_p \qquad\qquad (3)$$

The ion and electron densities for the conditions under consideration are shown in Figure 5.3c. The ion density is obtained by fitting the IV probe characteristic, in the ion saturation regime, to the well-known $(V_{probe} - V_{plasma})^{1/2}$ dependence described by OML theory. The electron density is obtained by integrating the measured EEDFs. For completeness, we also show the electron temperature T_e as a function of input power in Figure 5.3c. The

nanoparticle density n_p has been measured using laser light scattering (LLS) from a continuous wave 532 nm solid-state laser.
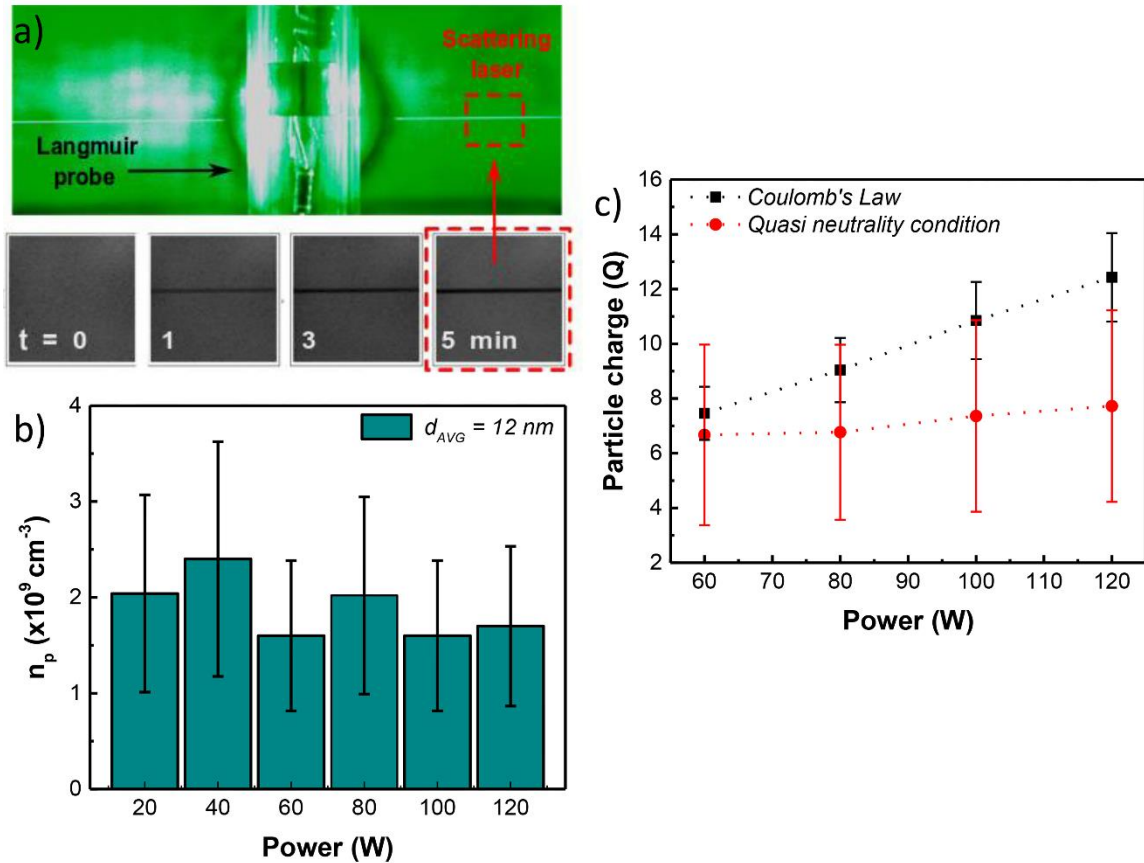
Figure 5.5. Picture showing the laser scattering from the graphitic carbon particles injected in the primary chamber (a). The inset shows an image sequence of the scattering line as a function of time, highlighting the building up of the particle-trapping phenomenon. Trapped nanoparticle density as a function of plasma power (b). Absolute value of the particle charge as a function of the applied RF power calculated from the plasma charge deficit and the particle potential (c).

In Figure 5.5a we show a photograph of the intense laser line which can be distinguished even by naked eye. Photographs of the laser beam at different times 't' are also shown in the same figure. Here 't' is the time delay from when the plasma in the primary chamber is ignited. At t = 0, i.e. when the plasma has not been ignited yet, the

scattering from the laser line is not visible. The scattering intensity increases after the plasma is ignited, stabilizes within few minutes and become clearly distinguishable even by naked eye. This suggests that significant particle trapping is occurring, with the density of particles in the plasma slowly increasing to a steady state value. A 90° optical configuration was used to collect the scattered laser intensity, defined as $I_p = I_0\, n_p\, \sigma_p$, where I_o is the incident intensity of the laser, n_p is the particle density and σ_p is the scattering cross section a carbon particle.[16] The value of n_p was then calculated from Eq (3). A detailed description of the Rayleigh spectra processing is shown in the Experimental section of the manuscript. In the calculation, the effective Rayleigh scattering cross-section σ_p was calculated by convoluting over the Gaussian fit of the particle size distribution in Figure 5.3a. This is necessary given the $(2R)^6$ dependence of the scattering cross section over particle diameter, $2R$.[16] The particle density n_p as a function of plasma power of the primary chamber is shown in Figure 5.5b. We find a value of $\sim 2\times10^9$ cm^{-3}, with no statistically meaningful dependence over plasma power. We have also measured the nanoparticle injection rate from the particle producing cell to the primary chamber. This has a value of 1.6 mg/hour, from which we can estimate a nanoparticle density of $\sim 10^7$ cm^{-3} if no trapping was present. The fact that the scattering signal increases considerably when the primary plasma is ignited, and the fact that the measured nanoparticle density is significantly higher than what is predicted by the mass balance, confirms that nanoparticle trapping is relevant in this system, and must be accounted for when calculating the average particle charge using equation (4).

In Figure 5.5c we show the particle charge calculated according to two different approaches. In the first, the average particle charge was calculated using Eq. (4) from the quasi-neutrality condition. The average charge has a weak dependence on power, with a value between 6 and 7 elementary charges per particle. This is in reasonable agreement with theoretical predictions, although we point out that the error bar in this measurement is significant. At 120 W of input power, Q is expected to be in the broad range between 4 and 11 charges per particle. This is a consequence of cumulative errors in the measurement of ion and electron densities, and most importantly in the measurement of the nanoparticle density, with uncertainty in the scattering cross section being the dominant source of uncertainty (see Figure 5.5b). Estimating the nanoparticle size via TEM is notoriously imprecise, and the 6th-power dependence of cross section over particle size amplifies the error in the determination of the optical cross section.

In Figure 5.5c we also show the particle charge assuming that the peaks in the EEPFs shown in Figure 5.3b are due to electrons emitted from the nanoparticles, and that the peak position corresponds to the nanoparticle floating potential derived from Coulomb's law, $\Phi = Z_k /(4 \pi \varepsilon R)$, with $Z_k = Qe$ (where e is the electron charge, ε is the vacuum permittivity, and Q is number of elementary charges per particle). The results obtained via this approach are in reasonable agreement at low input power with a more significant deviation at higher power. The error bar for this measurement is also significantly smaller than when using quasi-neutrality, mainly because this method does not require the calculation of the laser scattering cross section. We also stress that we are neglecting any possible nanoparticle agglomeration effect in the plasma, which would

lower the nanoparticle density and result in a larger charge when using equation (4). The reasonable agreement between these two approaches to determining nanoparticle charge offers some partial validation to the hypothesis that the peak in the EEPF is due to the nanoparticles dispersed in the plasma. Additional validation is provided by Kamran Shojaei, with his work on a self-consistent model for the theoretical prediction of the EEPF in dusty plasmas which accounts for the effect of electron emission from dust. The model is based on the freeware software Bolos, which provides a solution of energy probability function via a two-term approximation of the Boltzmann Transport Equation (BTE) under steady state.[23, 24] This solver requires as an input the reduced electric field E/N, the gas phase composition in terms of argon, hydrogen and nanoparticle densities, and the appropriate collision cross sections. We stress that the collision cross sections for the particles strongly depend on their floating potential. The cross sections for elastic and inelastic processes for argon and hydrogen are taken from LxCat database. [25] The elastic cross-section for the nanoparticles is determined by a Coulomb scattering process, and the attachment cross-section, that is electrons collected by the particles, is zero for energies below the nanoparticle floating potential as electrons cannot overcome the potential barrier induced by the negative charge on the nanoparticle. The expressions for both elastic and attachment cross-sections were obtained from Khrapak et. al.[26] leading to this expression:

$$\sigma_{coll} = \begin{cases} \pi R^2 (1 + \dfrac{\Phi}{E}), & E > -\Phi \\ 0, & E \leq -\Phi \end{cases} \qquad (5)$$

Electron emission is accounted for through the introduction of a detachment cross-section for the nanoparticles with the following expression:

$$\sigma_{det\,ach} = \frac{b}{\sqrt{\pi}} exp\left[-\left(\frac{E - |\Phi|}{a}\right)^2\right] \quad (6)$$

This detachment cross-section is effectively assuming that the electrons are emitted from nanoparticles with an energy equivalent to their floating potential, Φ. Two fitting parameters are introduced to investigate the effect electron emission has on the theoretical EEPF, a controlling the width of the function (e.g., the distribution of potential) and b controlling the magnitude of the detachment. The frequency of the attachment and detachment of electrons to/from particles is calculated using (5) and (6) and averaging over the EEPF obtained numerically; at steady state, Kirchoff's Law constrains the charge collection to:

$$\nu_{ion} + \nu_{e-det\,ach} = \nu_{e-attach} \quad (7)$$

And allows for the introduction of a detachment proportionality factor, δ, defined as:

$$\nu_{e-detatch} = \delta\nu_{ion} \quad (8)$$

The results of this work by Kamran Shojaei which further validate the hypothesis that these particles act as distributted electron emitters are detailed in Figure 5.6. Figure 5.6a shows the effect of scaling δ from 0 to 0.95; as is expected, δ = 0 results in no distinguishable peak in the EEPF and increasing values of δ lead to the emergence of a peak in the EEPF between 1 and 2 eV above the plasma potential, corresponding to the nanoparticle floating potential.
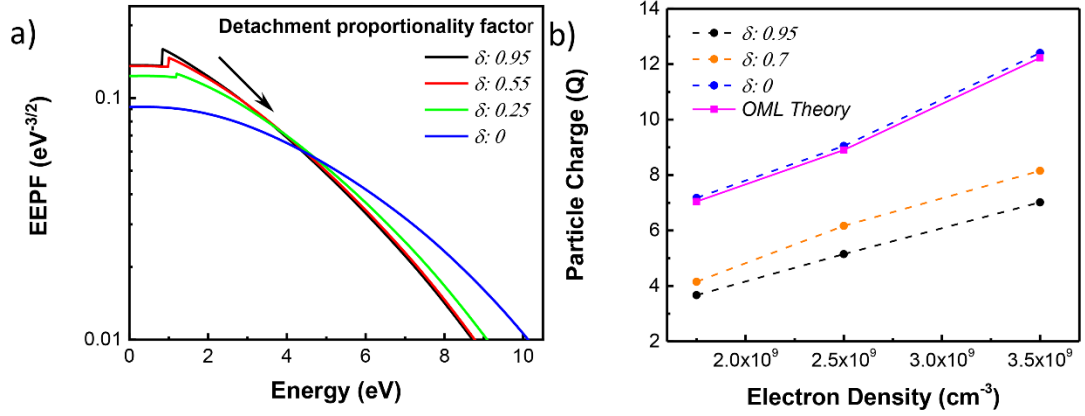
Figure 5.6. (a) EEPFs calculated for different values of electron emission parameter. (b) Absolute value of the particle charge as a function of electron density as predicted by the OML theory and for increasing values of the electron emission parameter.

In Figure 5.6b, the particle charge predicted by OML theory and calculated through Kamran's self-consistent model are compared; as expected, when $\delta = 0$, the two approaches are in good aggreement, with the number of charges dropping drastically with increasing δ. Overall, this model supports the hypothesis that a peak in the EEPF emerges due to to dust inside the discharge volume and can be tied to the injection of electrons into the plasma with kinetic energies equal to the floating potential of the nanoparticles.

5.4 Conclusions

In conclusion, we have performed careful measurements of the EEDF in a low-pressure dusty plasma and observed the appearance of a peak in the distributions. Optical measurements of laser scattering have confirmed the phenomenon of nanoparticle trapping, leading to an increase of the nanoparticle density from ~10^7 cm^{-3} to ~10^9 cm^{-3}. This trapped density was used to calculate the particle charge from Eq. (4), which was found to be in

reasonable agreement with the expected particle charge upon assuming the 2-3 eV peak in the EEDF is representative of the nanoparticle floating potential, thus offering some validation to the hypothesis that the observed peak is attributed to the nanoparticles acting as distributed electron emitters. A self-consistent model has been developed to investigate how the presence of the particles affects the EEDF, in particular to account for the emission of electrons from the nanoparticles. The good qualitative agreement between the measurements and the calculations supports the aforementioned hypothesis, leading to the appearance of a peak in the EEDF that corresponds to the nanoparticle floating potential. This work provides the first direct electrical measurement of the nanoparticle floating potential in a dusty plasma and represents a step towards understanding the complex coupling between plasmas and nanoparticles dispersed within it.

5.5 References

(1) Selwyn, G. S., Weiss, C. S., Sequeda, F., and Huang, C., *J. Vac. Sci. Technol. A* **15**, 2023 (1997).

(2) Selwyn, G. S., Singh, J., and Bennett, R. S., *J. Vac. Sci. Technol. A* **7** , 2758 (1989).

(3) Firth, P., and Holman, Z. C., *ACS Appl. Nano Mat.* **1**, 4351 (2018).

(4) Chen, T., Reich, K. V., Kramer, N. J., Fu, H., Kortshagen, U. R., and Shklovskii, B. I., *Nat. Mater.* **15**, 299 (2015).

(5) Barragan, A. A., Nava, G., Wagner, N. J., and Mangolini, L., *J. Vac. Sci. Technol. B* **36**, 011402 (2018).

(6) Sinha, M., Izadi, A., Anthony, R., and Roccabianca, S., *Nanoscale* **11**, 7520 (2019).

(7) Exarhos, S., Barragan, A. A., Aytan, E., Balandin, A. A., and Mangolini, L., *ACS Energy Lett.* **3**, 2349 (2018).

(8) Barragan, A. A., Ilawe, N. V., Zhong, L., Wong, B. M., and Mangolini, L., *J. Phys. Chem. C* **121**, 2316 (2017).

(9) Nava, G., Fumagalli, F., Gambino, S., Farella, I., Dell'Erba, G., Beretta, D., Divitini, G., Ducati, C., Caironi, M., Cola, A., and Di Fonzo, F., *J. Mater. Chem. C* **5**, 3725 (2017).

(10) Nava, G., Fumagalli, F., Neutzner, S., and Di Fonzo, F., *Nanotechnology* **29**, 465603 (2018).

(11) Barragan, A. A., Hanukovich, S., Bozhilov, K., Yamijala, S. S. R. K. C., Wong, B. M., Christopher, P., and Mangolini, L., *J. Phys. Chem. C* **123**, 21796 (2019).

(12) Lopez, T. and Mangolini, L., *J. Vac. Sci. Technol*. **32**, 061802 (2014).

(13) Schramke, K. S., Qin, Y., Held, J. T., Mkhoyan, K. A., and Kortshagen, U. R., *ACS Appl. Nano Mat.* **1**, 2869 (2018).

(14) Godyak, V. A., Piejak, R. B., and Alexandrovich, B. M., *J. Appl. Phys.* **73**, 3657 (1993).

(15) Woodard, A., Shojaei, K., Nava, G., and Mangolini, L., *Plasma Sources Sci. T.* **27**, 104003 (2018).

(16) Moosmüller, H., and Arnott, W. P., *J. Air Waste Manage.* **59**, 1028 (2009).

(17) Sneep, M., and Ubachs, W., *J.Quant. Spectrosc. Ra.* **92**, 293 (2005).

(18) Woodard, A., Shojaei, K., Nava, G., and Mangolini, L., *Plasma Chem. Plasma P*. **38**, 683 (2018).

(19) Klindworth, M., Arp, O., and Piel, A., *Rev. Sci. Instrum.* **78**, 033502 (2007).

(20)   Bilik, N., Anthony, R., Merritt, B. A., Aydil, E. S., and Kortshagen, U. R., *J.Phys. D Appl. Phys.* **48**, 105204 (2015).

(21)   Druyvesteyn, M. J., *Zeitschrift für Physik* **64**, 781 (1930).

(22)   DeJoseph Jr., C. A., Demidov, V. I., and Kudryavtsev, A. A., *Phys. Plasmas* **14**, 057101 (2007).

(23)   Hagelaar, G. J. M., and Pitchford, L. C., *Plasma Sources Sci. T*. **14**, 722 (2005).

(24)   *Bolos: Boltzmann equation solver open sources library*. Available from: https://github.com/aluque/bolos

(25)   *UNAM database*. Available from: www.lxcat.net.

(26)   Khrapak, S. A., and Morfill, G. E., *Phys. Rev. E* **69**, 066411 (2004).

Chapter 6: General Conclusions and Outlook

The work presented in this dissertation forms a solid groundwork for further expanding on the understanding of plasma-dust interactions and the effect of such on plasma behavior. Rather than probing plasma environments which contain insulating or semiconducting nanoparticles, deliberate design of a system which contains conductive dust fosters a more forgiving environment for Langmuir probe investigations; furthermore, specifically a system that contains no extraneous elements, such as reactive gases remaining from any synthesis technique employed. Using a non-thermal plasma synthesis technique enables the synthesis of the conductive dust with full consumption of precursor molecules, resulting in an output of dust and inert gases.

Chapter 2 is the first attempt at designing a system for the synthesis of conductive dust, through a non-thermal plasma reactor with $Ni(Cp)_2$ as precursor. The results presented here show that a continuous flow non-thermal plasma reactor can synthesize metallic Ni nanoparticles, while maintaining substantial control of the produced dust with respect to chemical composition, particle size distribution, and crystallinity. Unfortunately, with respect to this dissertation's goal of synthesizing simple conductive dust without remaining precursor molecules, this attempt falls short. The synthesized dust is of a core-shell Ni-C structure, with unavoidable secondary contaminants in the form of carbonaceous nanoparticles; additionally, although the addition of hydrogen in the gas mixture reduces the amount of contaminant, it is not fully eradicated and thus is an indication of remaining precursor molecules. Further investigations are encouraged regarding the possibility of

using similar processes to see if there exists any differences on the plasma-dust interaction based on the dust's structure and chemical composition.

Chapter 3 presents a non-thermal plasma synthesis method of synthesizing graphitic carbon nanoparticles, inspired by the unavoidable contaminant found in Chapter 2. The results show that using this synthesis method, a high degree of control over the degree of graphitization can be achieved, with in-situ FTIR measurements showing particle incandescence as the dust transitions from amorphous to highly graphitic, and RGA measurements confirming the complete consumption of the precursor gas. Thus, this synthesis method satisfies one of the main design goals of this dissertation, providing a method of independently producing conductive nanoparticles that are pure in composition while consuming the entirety of the precursor gas, outputting only the conductive dust and inert gas. Further work on exploring the full capabilities of this system to synthesize an entire family of carbonaceous nanoparticle structures would be of interest for understanding the role of the dust structure on plasma-dust interaction as well, similar to that stated above.

Chapters 4 and 5 detail the results of employing a homemade Langmuir probe device in a dusty plasma environment that, aided by Chapter 2, only contains conductive nanoparticles and inert gas. Chapter 4 investigates the effects of plasma-dust interactions on the EEPF (and therefore the plasma parameters) at a relatively high pressure of 150 mTorr, confirms the functionality of the homebuilt Langmuir probe in an pristine Ar-only environment while uncoated and coated with a thick layer of the graphitic nanoparticles, as well as establishes what the dominant ion is expected to be in the $Ar-H_2$ discharge used

in this chapter. The theoretical expectation of the addition of dust resulting in a decreased n_e and increased T_e is confirmed; a simplistic particle charging model is used, accounting for thermionic emission from the nanoparticles, to corroborate the results found with respect to particle charge acquired inside the plasma. Chapter 5 extends this study to a much lower pressure regime, 15 mTorr, while incorporating optical emission measurements of laser scattering as well as a much more robust self-consistent model for understanding how the presence of particles affects the EEDF. An unexpected appearance of a peak in the EEDF is observed. The optical emission measurements confirm the phenomenon of nanoparticle trapping, leading to an increase of n_p from $\sim 10^7$ cm^{-3} to $\sim 10^9$ cm^{-3}. This increased nanoparticle density was used to calculate the particle charge and was in reasonable agreement with the expected particle charge upon assuming the observed peak in the EEDF is indicative of the nanoparticle floating potential. The self-consistent model is able to successfully recreate the emergence of the peak in the EEDF, with good qualitative agreement between the experimental measurements and the calculations from the model. Further work should be on investigating the effects of dust chemical composition. A thermal evaporation system designed to produce metallic nanoparticles, such as copper, gold, or silver, could be an interesting alternative synthesis technique to replace the current graphitic nanoparticle producing method. In addition, the model should be strengthened to fully couple how the plasma-dust interactions, such as particle heating, effect the rate of electron emission from the particle surface, rather than assuming a variable constant parameter.